*J. Fluid Mech.* (2021), *vol*. 916, A11, doi:10.1017/jfm.2021.200

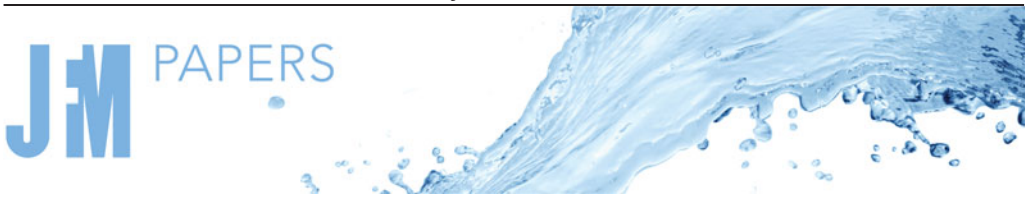


# Scattering of flexural-gravity waves by a crack in a floating ice sheet due to mode conversion during blocking

**S.C. Barman[1], S. Das[2,†], T. Sahoo[1] and M.H. Meylan[3]**

[1]Department of Ocean Engineering and Naval Architecture, Indian Institute of Technology Kharagpur, Kharagpur 721302, India

[2]Mathematical and Computational Sciences Division, Institute of Advanced Study in Science and Technology, Guwahati 781035, India

[3]School of Mathematical and Physical Sciences, University of Newcastle, NSW 2308, Australia

(Received 19 March 2020; revised 24 January 2021; accepted 2 March 2021)

The scattering of flexural-gravity waves in a thin floating plate is investigated in the presence of compression. In this case, wave blocking occurs, which is associated with both a zero in the group velocity and coalition of two or more roots of the related dispersion relation. There exists a region in the frequency space in which there are three real roots of the dispersion equation and hence three propagating modes. This multiplicity leads to mode conversion when scattering occurs. In one of these modes, the energy propagation direction is opposite to the wavenumber, making enforcement of the Sommerfeld radiation condition challenging. The focus here is on a canonical problem in flexural-gravity wave scattering, the scattering of waves by a crack. Formulae are developed that apply uniformly at all frequencies, including through the blocking frequencies. This solution is developed by tracking the movement of the dispersion relation roots carefully in the complex plane. The mode conversion is verified by the scattering matrix of the process and through an energy identity. This energy identity for the case of more than one progressive modes is established using Green's theorem and later applied in the scattering matrix to identify the incident and transmitted waves in the scattering process and derive the radiation condition. Appropriate scaling of the reflection and transmission coefficients are provided with the energy identity. The solution method is illustrated with numerical examples.

**Key words:** wave–structure interactions, wave scattering, ice sheets

† Email address for correspondence: santudas20072@gmail.com

## 1. Introduction

The problem of determining the effect that a floating elastic plate has on surface wave propagation has been the subject of extensive research due to its application to polar oceanography and marine engineering (Squire 2018, 2020). The first solution to this problem was given by Kouzov (1963), who provided a solution to the problem of hydroelastic waves scattered by two thin elastic plates with identical properties separated by a crack. The integral representation was used to reduce the mathematical problem to a Riemann–Hilbert problem, and it was explicitly solved. Later, Fox & Squire (1990, 1994) analysed the scattering of ocean waves by shore fast sea ice modelled as a semi-infinite elastic plate in the case of finite depth water by applying appropriate matching conditions across the interface and the conjugate gradient method. Barrett & Squire (1996) obtained a numerical solution to the problem of a single crack in an otherwise infinitely extended ice sheet for the case of finite depth ocean extending the previous method. Later, Squire & Dixon (2000) applied a Green's function approach to study the ice-coupled wave propagating across an open crack in water of infinite depth. Further, Evans & Porter (2003) analysed the problem of scattering of obliquely incident waves caused by a narrow crack in an ice sheet floating on water of finite depth by the eigenfunction expansion method as well as the Green's function approach to obtain simple expressions for the solution. Recently, there has been continued interest in solving for wave scattering by cracks or closely related problems involving walls or abrupt changes in properties (see Korobkin, Malenica & Khabakhpasheva 2018; Li, Wu & Ji 2018*a*,*b*; Shi, Li & Wu 2019; Ren, Wu & Li 2020).

One of the significant difficulties in dealing with problems related to wave interaction with floating elastic plates is the existence of higher-order boundary conditions associated with the flexible surface. The associated eigenfunctions are not orthogonal in the usual sense. The genesis of such expansion formulae is the classical wavemaker theory developed by Havelock (1929), who used the Laplace equation as the governing equation in water of finite and infinite depths with a Robin-type boundary condition on the mean free surface. The first extension of the wavemaker theory of Havelock (1929) was to the case of surface tension in which the boundary condition on the mean free surface becomes third order. Consequently, the boundary value problem is no longer of the Sturm–Liouville type. The corresponding expansion formulae for both the finite and infinite depth domains were derived by Rhodes-Robinson (1971), and the infinite depth case was later extended in the presence of vertical boundary (Rhodes-Robinson 1979). Sahoo, Yip & Chwang (2001) generalized the expansion formula for water of finite depth to analyse wave scattering generated by a semi-infinite elastic plate, where the boundary condition on the plate-covered surface is of fifth order. They used the eigenfunction expansion method and a newly developed orthogonal mode-coupling relation. Subsequently, Evans & Porter (2003) derived several properties of the eigenfunctions associated with the flexural-gravity waves. Manam, Bhattacharjee & Sahoo (2005) established the general expansion formulae and related orthogonal mode-coupling relations associated with flexural-gravity wave problems based on the application of Fourier analysis in both the cases of a semi-infinite strip and quarter plane to tackle a general class of boundary value problem in both the cases of water of finite and infinite depths. Mondal, Mohanty & Sahoo (2013) generalized the expansion formulae for wave–structure interaction problems in three dimensions in a homogeneous fluid. Mandal, Sahoo & Chakrabarti (2017) studied the convergence of the expansion formulae associated with wave–structure interaction problems of a single-layer fluid having a plate-covered surface. Unlike the case of wave–structure interaction problems discussed here, similar results have been established by Lawrie &

Abrahams (1999), Lawrie (2007) and Lawrie (2009) in acoustic wave interaction with a flexible structure in which the associated governing equation is the Helmholtz equation.

The governing equation of motion for an elastic plate can be augmented by the addition of a compressive stress term. Such stress is well known to exist in floating ice, and it has been suggested as a possible cause of ice break up (Liu & Mollo-Christensen 1988). The primary sources of such compression are thermal strain, high-speed wind over the plate and a current underneath the plate. This effect of the compressive stress has been the subject of study over a significant period of time, starting with Bukatov (1980). Further details on the buckling of a floating ice sheet can be found in Kerr (1983), where the connection between the critical compressive force for which buckling occurs is related to the vanishing of the phase velocity. Subsequent progress on this aspect includes the works of Davys, Hosking & Sneyd (1985), Schulkes, Hosking & Sneyd (1987), Liu & Mollo-Christensen (1988), Bukatov & Zav'yalov (1995), Squire *et al.* (2012) and Collins, Rogers & Lund (2017). One fundamental change observed in the presence of compression is due to the occurrence of wave blocking (Das, Sahoo & Meylan 2018*b*). This happens when the group velocity becomes zero. There exists a critical value of the compressive stress for which blocking is initiated, referred to as the threshold of blocking. This threshold can be identified by the existence of an inflexion point in the dispersion graph ($k$–$\omega$ plane, where $k$ is the wave number and $\omega$ is the frequency). At this blocking point, the associated group velocity vanishes. As the compressive stress increases, we reach a critical value known as the buckling limit where the plate is unstable, analogous to the well-known buckling limit of a finite beam. With an increase in the compressive stress between the threshold of blocking and the buckling limit, the point of inflexion bifurcates into two blocking points. Between these two blocking frequencies, waves with negative group velocity propagate and are confined therein. Within the blocking limits, the dispersion relation possesses three positive real roots, two of which coalesce at the point of blocking. In contrast, all of them coalesce at the point of inflexion. Such blocking occurs for surface tension and shear current (see Maïssa, Rousseaux & Stepanyants 2016). This also happens for flexural-gravity waves in a two-layer fluid having a plate-covered surface and an interface (Das, Sahoo & Meylan 2018*c*) and flexural-gravity waves in a shear current (Das *et al.* 2018*a*).

In the present study, we solve for scattering by a crack in an infinitely extended floating ice sheet in the presence of compression, focussing on the case when we have wave blocking. In this manuscript, often the floating ice sheet is referred to as a flexible plate. In this case, there exist multiple travelling waves for a given incident frequency. The scattering is complicated by this multiplicity and by the presence of waves with a negative group velocity. The outline of the manuscript is as follows. In § 2 we provide the mathematical formulation for the flexural-gravity wavemaker problem which will help us to build up the boundary value problem discussed in § 3. The solution process for the scattering problem is described in § 4 for distinct roots of the dispersion relation under both infinite and finite depth water domains. The energy conservation in the case when there is more than one propagating mode is derived in § 5 with the help of Green's theorem. § 6 details the method by which the scattering through the blocking frequency can be computed. The plate deflection is graphically illustrated in § 7. The manuscript ends with a brief conclusion in § 8.

## 2. Flexural-gravity wavemaker problem

The wavemaker problem represents the response of a fluid-filled domain with a free surface subject to the small amplitude oscillatory motion of a vertical wall along which

an arbitrary velocity distribution is imposed. It is a crucial problem and forms the basis for all eigenfunction matching methods in a finite depth fluid domain. A flexural-gravity wavemaker problem can physically be thought of as an equivalent problem when the free surface is covered with an elastic plate. When the depth of the fluid domain extends to infinity, the solution process depends on an integral of a function very similar to eigenfunctions for finite depth domain. In this section, the flexural-gravity wavemaker is considered for both finite and infinite water depths assuming linearized water wave theory and small amplitude response. The physical problem is considered in the two-dimensional Cartesian coordinate system. The fluid is assumed to be inviscid and incompressible, and the flow is irrotational and simple harmonic in time with angular frequency $\omega$ which ensures the existence of a velocity potential $\Phi(x, y, t)$ of the form $\Phi(x, y, t) = \mathrm{Re}\{\phi(x, y)\,\mathrm{e}^{-\mathrm{i}\omega t}\}$. We follow the assumption that the $x$-axis is horizontal and the $y$-axis is vertically downward positive. The fluid region in the case of finite depth is the semi-infinite strip $0 < x < \infty$ and $0 < y < h$, whilst for infinite depth is the quarter plane $0 < x < \infty$ and $0 < y < \infty$. The spatial velocity potential $\phi(x, y)$ satisfies the partial differential equation

$$\nabla^2\phi = 0, \quad \text{in the fluid domain.} \tag{2.1}$$

On the structural boundary, the spatial velocity potential $\phi(x, y)$ satisfies the boundary condition as given by (as in Schulkes *et al.* 1987)

$$\left(D\frac{\partial^4}{\partial x^4} + Q\frac{\partial^2}{\partial x^2} + 1 - \gamma gK\right)\frac{\partial\phi}{\partial y} + K\phi = 0 \quad \text{at } y = 0, \quad 0 < x < \infty, \tag{2.2}$$

where $D = EI/\rho g$, $Q = N/\rho g$, $K = \omega^2/g$, $E$ is Young's modulus, $I = d^3/12(1 - \nu)$, $d$ is plate thickness, $\nu$ is Poisson's ratio, $N$ (Newton $\mathrm{m}^{-1}$) is uniform compressive stress, $\rho$ is water density, $\gamma = \rho_i d/(\rho g)$, $g$ is the gravitational constant and $\rho_i$ is the density of the plate. It may be noted that the ice is routinely broken from stress forming ice ridges and ice keel. Therefore, the stress in compressed ice must be very high in such cases and the same high stress is considered for the study. The rigid bottom boundary (for finite depth)/no flux and boundedness (for infinite depth) condition(s) is/are given by

$$\left.\begin{array}{ll} \phi_y = 0 \text{ on } y = h & \text{in the case of finite depth,} \\ \phi, \mid \nabla\phi \mid \to 0 \text{ as } y \to \infty & \text{in case of infinite depth.} \end{array}\right\} \tag{2.3}$$

Further, on the vertical boundary at $x = 0$, the velocity potential $\phi(x, y)$ satisfies the conditions given by

$$\phi(0, y) = u(y), \tag{2.4}$$

and

$$\phi_x(0, y) = v(y). \tag{2.5}$$

where $u(y)$ and $v(y)$ are the prescribed functions to be introduced later.

Finally, the far-field radiation condition is given by

$$\lim_{x\to\infty}\left(\frac{\partial\phi}{\partial x} - \mathrm{i}k_0\phi\right) = 0, \tag{2.6}$$

where $k_0$ is the wavenumber associated with the plane wave solution which satisfies the dispersion relation in $k$ as given by

$$H(k) = 0, \tag{2.7}$$

where in finite depth

$$H(k) = \frac{k(Dk^4 - Qk^2 + 1)\tanh(kh)}{1 + \gamma gk\tanh(kh)} - K, \tag{2.8}$$

and in infinite depth

$$H(k) = \begin{cases} \dfrac{k(Dk^4 - Qk^2 + 1)}{1 + \gamma gk} - K, & \mathrm{Re}(k) > 0. \\ \dfrac{-k(Dk^4 - Qk^2 + 1)}{1 - \gamma gk} - K, & \mathrm{Re}(k) < 0. \end{cases} \tag{2.9}$$

The unique velocity potential can be obtained with specific $u(y)$ and $v(y)$ by solving the above boundary value problem with the help of appropriate edge conditions associated with the flexible plate which depend on the nature of the physical problems under consideration (see Sahoo *et al.* 2001; Manam *et al.* 2005).

The expansion formulae will be briefly discussed in the cases of infinite and finite water depths when the dispersion relation possesses distinct roots. The dispersion relation for finite water depth is an even function of $k$. In the absence of compression, it contains two real roots of the opposite sign, infinitely many imaginary roots and four complex roots. A similar convention for the location of the roots is utilized here when the ice sheet is compressed. In the case of infinite depth, there is a branch cut on the imaginary axis, and this branch cut replaces the roots on the imaginary axis (which become dense as the depth tends to infinity). A detailed analysis of the roots' location can be found in Squire & Dixon (2000), and in appendix B of Williams (2006), where the movement of the complex-valued roots towards either the real or imaginary axis under specific conditions is also described. We denote the positive real root as $k_0$ and the complex roots as $\pm k_I$ and $\pm k_{II}$ where $k_{II} = \bar{k}_I$ (overbar represent complex conjugate) with $k_I$ having positive real and imaginary parts.

It is worth mentioning that the inclusion of water compressibility into the formulation changes the dispersion relation slightly and results in a conversion of some of the roots located in the imaginary axis into the real axis (Abdolali *et al.* 2018). These newly formed waves are called acoustic-gravity waves that have an oscillatory profile in the vertical direction, unlike gravity waves, which have an oscillatory profile in the horizontal direction. However, incorporating water compressibility as a part of the present problem will deviate from the primary goal of studying the scattering of flexural-gravity waves. We deem it suitable for separate treatment and is thus not attempted for the time being.

The velocity potential $\phi(x, y)$ associated with the boundary value problem (BVP) satisfying (2.1)–(2.4) and (2.6) is expressed as (see Theorem 2.4 of Manam *et al.* 2005)

$$\phi(x, y) = A_0 f_0(y)\,\mathrm{e}^{\mathrm{i}k_0 x} + A_I f_I(y)\,\mathrm{e}^{\mathrm{i}k_I x} + A_{II} f_{II}(y)\,\mathrm{e}^{-\mathrm{i}k_{II} x} + \frac{2}{\pi}\int_0^\infty \frac{A(\xi)M(\xi, y)\,\mathrm{e}^{-\xi x}\,\mathrm{d}\xi}{\Delta(\xi)}, \tag{2.10}$$

with

$$\left.\begin{aligned} A_n &= \frac{1}{C_n}\int_0^\infty u(t) f_n(t)\,\mathrm{d}t + \frac{k_n}{KC_n}\left[(Q - Dk_n{}^2)\phi_y - D\phi_{yyy}\right]_{(x,y)=(0,0)},\\ A(\xi) &= \int_0^\infty u(t) M(\xi, t)\,\mathrm{d}t + \xi\left[(Q + D\xi^2)\phi_y - D\phi_{yyy}\right]_{(x,y)=(0,0)},\\ M(\xi, y) &= \xi\left(D\xi^4 + Q\xi^2 + 1 - g\gamma K\right)\cos\xi y - K\sin\xi y,\\ \Delta(\xi) &= \xi^2\left(D\xi^4 + Q\xi^2 + 1 - g\gamma K\right)^2 + K^2,\\ f_n(y) &= \mathrm{e}^{-k_n y}, \quad C_n = \frac{H'(k_n)}{2K} \quad \text{for } n = 0, I, II. \end{aligned}\right\} \tag{2.11}$$

Similarly, when the velocity potential $\phi(x, y)$ satisfies condition (2.5) instead of (2.4), $A_n$ and $A(\xi)$ in (2.10) are given by

$$\left.\begin{aligned} A_n &= \frac{-\mathrm{i}\epsilon_n}{C_n k_n}\left\{\int_0^\infty v(t) f_n(t)\,\mathrm{d}t + \frac{k_n}{K}\left[(Q - Dk_n{}^2)\phi_{xy} - D\phi_{xyyy}\right]_{(x,y)=(0,0)}\right\},\\ A(\xi) &= \frac{-1}{\xi}\left\{\int_0^\infty v(t) M(\xi, t)\,\mathrm{d}t + \xi\left[(Q + D\xi^2)\phi_{xy} - D\phi_{xyyy}\right]_{(x,y)=(0,0)}\right\},\\ \epsilon_n &= \begin{cases} 1 & \text{for } n = 0, I,\\ -1 & \text{for } n = II. \end{cases} \end{aligned}\right\} \tag{2.12}$$

The eigenfunctions $f_n(y)$ $(n = 0, I, II)$ and the kernel $M(\xi, y)$ in (2.10) satisfies the orthogonal mode-coupling relation given by Manam *et al.* (2005)

$$\langle f_m(t), f_n(t)\rangle = \begin{cases} C_n & \text{for } m = n,\\ 0 & \text{otherwise,} \end{cases} \tag{2.13}$$

where

$$\begin{aligned} \langle f_m(t), f_n(t)\rangle = &\int_0^\infty f_m(t) f_n(t)\,\mathrm{d}t - \frac{Q}{K}\left[f_m'(t) f_n'(t)\right]_{t=0}\\ &+ \frac{D}{K}\left[f_m'''(t) f_n'(t) + f_m'(t) f_n'''(t)\right]_{t=0}. \end{aligned} \tag{2.14}$$

Further, it can be easily derived that

$$\langle M(\xi, t), f_n(t)\rangle = 0 \quad \text{for } n = 0, I, II. \tag{2.15}$$

It may be noted that the kernel $M(\xi, y)$ satisfies various identities as mentioned in Lemma 2.5 of Mondal *et al.* (2013). Moreover, the unknowns, $A_n$ and $A(\xi)$, can be obtained by using the orthogonal mode-coupling relation as defined in (2.13) and (2.15).

In a similar manner, the velocity potential $\phi(x, y)$ in the case of finite water depth, satisfying (2.1)–(2.4) and (2.6), is obtained as

$$\phi(x, y) = A_0\, \mathrm{e}^{\mathrm{i}k_0 x} f_0(y) + A_I\, \mathrm{e}^{\mathrm{i}k_I x} f_I(y) + A_{II}\, \mathrm{e}^{-\mathrm{i}k_{II} x} f_{II}(y) + \sum_{n=1}^{\infty} A_n f_n(y)\, \mathrm{e}^{-k_n x}, \quad (2.16)$$

with

$$\left.\begin{aligned} A_n &= \frac{1}{C_n}\int_0^h u(t) f_n(t)\, \mathrm{d}t + \frac{k_n \tanh k_n h}{KC_n}\left[(Q - Dk_n{}^2)\phi_y - D\phi_{yyy}\right]_{(x,y)=(0,0)}, \\ C_n &= \frac{H'(k_n)\tanh k_n h}{2K} \quad \text{for } n = 0, I, II, 1, 2\ldots \quad \text{and} \quad k_n = \mathrm{i}k_n, \quad \text{for } n = 1, 2, 3, \ldots \end{aligned}\right\} \quad (2.17)$$

and the eigenfunctions

$$f_n(y) = \begin{cases} \dfrac{\cosh k_n(h - y)}{\cosh k_n h} & n = 0, I, II. \\ \dfrac{\cos k_n(h - y)}{\cos k_n h} & n = 1, 2, 3, \ldots, \end{cases} \quad (2.18)$$

Similarly, when the velocity potential $\phi(x, y)$ satisfies (2.5) instead of (2.4), the constants $A_n$ in (2.16) are obtained as

$$\left.\begin{aligned} A_n &= \frac{-\mathrm{i}\delta_n}{C_n k_n}\left\{\int_0^h v(t) f_n(t)\, \mathrm{d}t + \frac{k_n \tanh k_n h}{K}\left[(Q - Dk_n{}^2)\phi_{xy} - D\phi_{xyyy}\right]_{(x,y)=(0,0)}\right\}, \\ \delta_n &= \begin{cases} 1 & \text{for } n = 0, I, 1, 2, \ldots \\ -1 & \text{for } n = II. \end{cases} \end{aligned}\right\} \quad (2.19)$$

The orthogonal mode-coupling relation (see Manam *et al.* 2005) is given by

$$\begin{aligned} \langle f_m(t), f_n(t)\rangle &= \int_0^h f_m(t) f_n(t)\, \mathrm{d}t - \frac{Q}{K}\left[f_m'(t) f_n'(t)\right]_{t=0} + \frac{D}{K}\left[f_m'''(t) f_n'(t) + f_m'(t) f_n'''(t)\right]_{t=0}, \\ &= \begin{cases} C_n & m = n, \\ 0 & \text{otherwise.} \end{cases} \end{aligned} \quad (2.20)$$

The unknown coefficients, $A_n$, are also can be determined from the prescribed boundary conditions and the orthogonal mode-coupling relation defined in (2.20). Moreover, it may be noted that the orthogonal mode-coupling relation for wave–structure interaction problems in water of finite depth was initially defined by Sahoo *et al.* (2001). Various other characteristics of the eigensystem and convergence of the expansion formulae in both the cases of water of finite and infinite water depths have been discussed in Sahoo (2012) and Mandal *et al.* (2017). Moreover, in the above-mentioned expansion formula, it is assumed that the eigenvalues, $k_n$, are distinct roots of the dispersion relation (2.7) in both the cases of water of finite as well as infinite depths.

At this point, we would like to emphasize the influence of the plate compression on wave propagation by examining the dispersion relation provided in (2.7). Without loss of generality, the case of finite water depth is taken into account and plotted for four different values of plate compression – $Q/\sqrt{D} = 1.3$, 1.75, 1.95, 2, 2.02 and 2.04 along

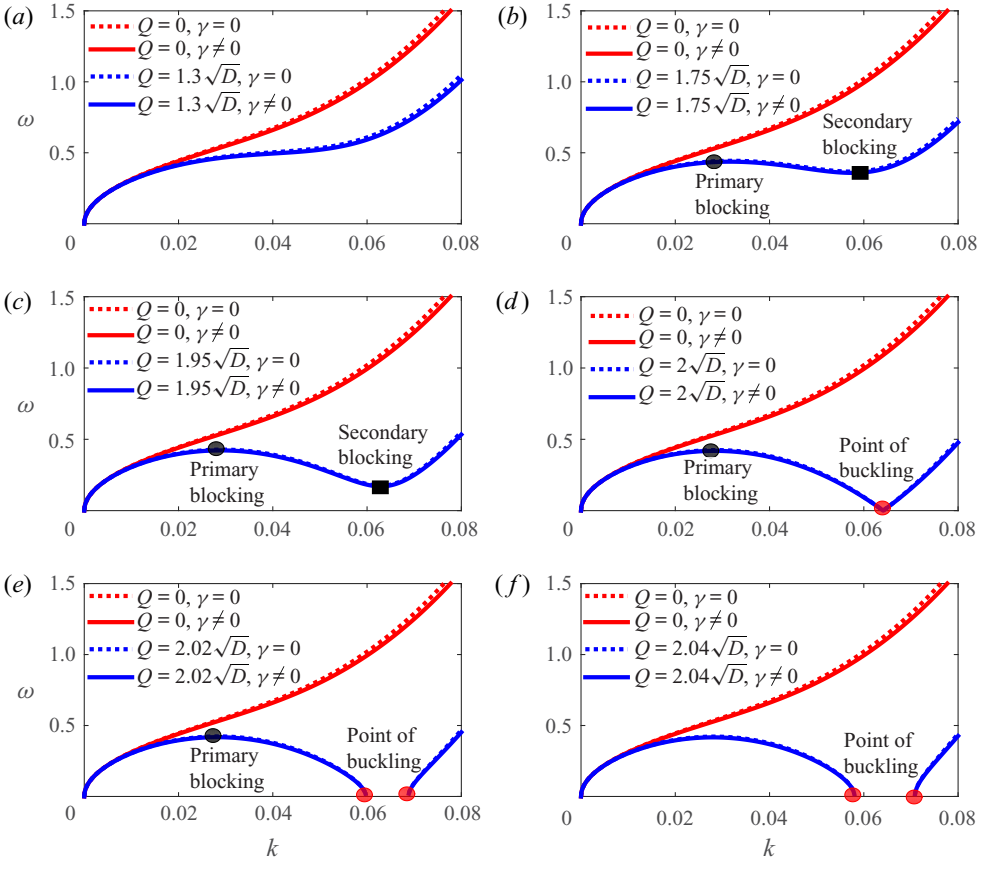


Figure 1. The evolution of dispersion graphs in finite water depth as plate compression increases is shown for six different values, namely $Q = 1.3\sqrt{D}$, $Q = 1.75\sqrt{D}$, $Q = 1.95\sqrt{D}$, $Q = 2\sqrt{D}$, $Q = 2.02\sqrt{D}$ and $Q = 2.04\sqrt{D}$, of compression juxtaposing with the uncompressed plate ($Q = 0$). The dotted curves are for the case when the inertial effect is ignored, whereas the rigid curves represent the inclusion of inertial effect. Ice thickness is kept at $d = 1$ m. The generation of primary and secondary blocking points and the point of buckling are visible. As we increase the compression above $2\sqrt{D}$, the point of buckling splits and starts moving along the $k$ axis. The wavenumber band between the buckling points does not attribute to any wave propagation irrespective of any incoming frequency. The change in the dispersion curve due to the inertial effect is rather much less.

with the case of no compression ($Q = 0$) to highlight the effect. A result for the particular approximation due to negligible inertial effect ($\gamma = 0$) is also presented in the graphs using the dotted curves. The physical parameter values used for the computational purpose are the same as provided in Meylan & Squire (1994) and are mentioned here for convenience: Young's modulus $E = 5$ GPa, Poisson's ratio $\nu = 0.3$, water density $\rho = 1025$ kg m$^{-3}$, ice density $\rho_i = 922.5$ kg m$^{-3}$, ice thickness $d = 1$ m and the gravitational constant $g = 9.81$ m s$^{-2}$. The nature of the graph, which is monotonically increasing for the uncompressed plate, evolves to produce optima with an increasing value of compression. The maximum occurring for higher frequency and lower wavenumber corresponds to the primary blocking. On the contrary, the minimum occurring for lower frequency and higher wavenumber is termed the secondary blocking point (see figure 1). At both these points, the group velocity (or the slope of the $k - \omega$ curve) vanishes so that the energy

propagation is zero. The dispersion relation possesses three positive real roots for any frequency between the primary and secondary blocking frequencies. With the increase in plate compression, the frequency band for having three real roots widens. One interesting observation is the occurrence of a sharp corner in the dispersion curve when $Q = 2\sqrt{D}$ due to discontinuity in the group velocity $(\mathrm{d}\omega/\mathrm{d}k)$ at that point. In terms of physical interpretation, the wave envelope is broken into two parts travelling in opposite directions – a phenomenon termed as 'buckling', representing physically the breaking of the plate. We briefly discuss the plate buckling. Under compression, a finite plate will buckle (small perturbations will grow) for a length-dependent function of compression. It is such a factor which determines the strength of columns under compression. For an infinite plate, the buckling will occur for any compression. In our case, there is an extra term due to the hydrostatic pressure (which acts to restore the plate to equilibrium), and this means that, even for an infinite plate, there is a critical compression before bucking occurs. A further increase in the compression splits the buckling point into two parts, and they will move away from each other along the wavenumber axis. We also note that Kerr (1983) has established a dependency between the vanishing of phase velocity and the mechanical failure due to buckling of the flexible plate. There will be a wavenumber band that widens with respect to an increasing compression and, in which no flexural-gravity wave can propagate irrespective of the incident wave frequency. A similar observation was also pointed out earlier by Das *et al.* (2018*b*).

We further demonstrate the effect of plate thickness on the blocking points in figure 2 with $d = 1$ m, 1.2 m, ..., 1.5 m and $\gamma = 0$ (i.e. ignoring the inertial term with $d = 1$ m). The value of compressive stress is kept fixed at $1.75\sqrt{D}$. The movement of the blocking points is visible as plate thickness increases. The action of ice thickness is to shift the blocking frequency as well as wavenumber (both primary and secondary) to a lower value, consequently, the frequency band of the multiple propagating modes shifts. The change in the position of primary and secondary blocking points is sufficiently small when the cases of $\gamma = 0$ and $\gamma \neq 0$ are compared. Although the thickness of sea ice alters the frequency band of blocking, the wave profile's qualitative nature remains the same. Thus the subsequent results presented in this work, except for the plate elevation, are performed with $\gamma = 0$. The effect of plate thickness is demonstrated in separate graphs whenever needed.

The roots of the dispersion relation (2.7) are qualitatively the same in both the finite and infinite water depth cases except for the evanescent modes. These evanescent modes are purely imaginary and have an insignificant effect on the scattering process, which form a continuum in the latter case. The movement of the roots in the complex plane with increasing values of incoming wave frequencies is graphically shown in figure 3 when the plate thickness is kept fixed at $d = 1$ m. As we increase the incoming wave frequency, the roots from the complex plane travel towards the real axis and merge to create the secondary blocking (see figure 3*b*). The merging happens for the complex roots $k_I$, $-k_{II}$ with $k_{II}$, $-k_I$, respectively, to generate the critical points $\pm k_c$ that bifurcate into real roots. In order to distinguish the newly generated real roots from the earlier complex ones, we term them as $\pm k_1$ and $\pm k_2$. Then these roots start travelling away from each other to create in total six distinct roots (see figure 3*c*,*d*). A further increase in frequency ensures a coalition of the two real roots to generate primary blocking (see figure 3*e*). The coalition occurs between the roots $\pm k_0$, $\pm k_2$ to create the critical points $\pm k_c'$. Finally, $\pm k_c'$ bifurcate to regenerate the complex roots $\pm k_I$, $\pm k_{II}$ back into the physical system (see figure 3*f*). Note that primary blocking is associated with high frequency waves having relatively smaller wavenumber compared to secondary blocking, which occurs for waves having a lower frequency and a

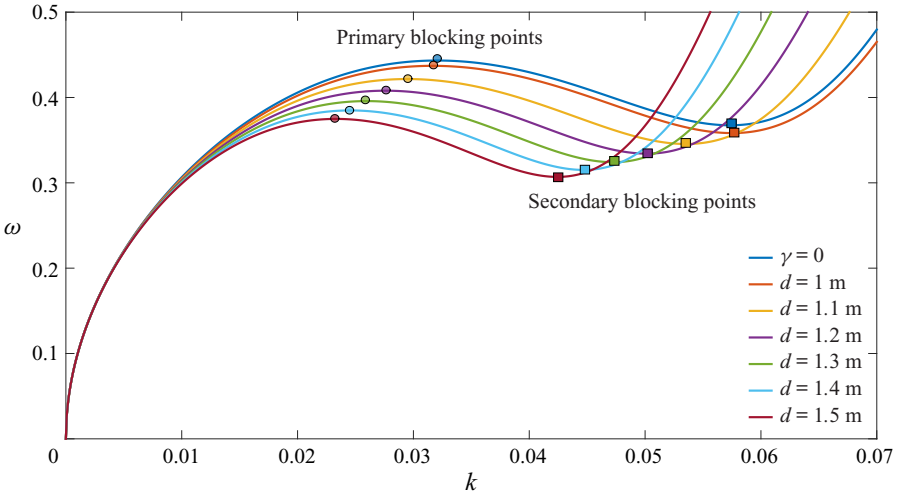


Figure 2. Variation of blocking points for different values of ice thickness along with $\gamma = 0$ (approximation due to negligible inertial effect with $d = 1$) is depicted here.

larger wavenumber. The same analysis of the dispersion graph is conveyed through figure 4 by a one-to-one relationship with the panels of figure 3.

## 3. Flexural-gravity wave scattering by a crack in a floating ice sheet

In the present section, as an application of the wavemaker problem in the case of water in infinite depth, the flexural-gravity wave scattering caused by a straight line crack in an ice sheet with compression is reinvestigated. However, the solution process is discussed in both the cases of finite and infinite water depths but limiting the corresponding analysis of wave scattering for the infinite water depth only to avoid repetition. It is worth mentioning, for brevity, that closed-form solutions are obtained elegantly following the method of Evans & Porter (2003) in the water of finite depth through the application of Green's integral theorem. We are analysing the behaviour of different modes of wave propagation close to the blocking frequencies in water of infinite depth using the approach of Manam *et al.* (2005), which was not discussed earlier. Specifically, the form for the potential function during the amalgamation of the two roots of the dispersion relation can be written with the help of the distinct roots in the given form of the velocity potentials. Various known results of physical importance available in the literature are reproduced from the analytical expressions.

The physical domain associated with the flexural-gravity wave scattering by a crack in a floating ice sheet remains similar to that discussed in the formulation earlier in § 2 except $-\infty < x < \infty$ and $0 \leqslant y < \infty$ and is exhibited in figure 5. Here, the ice sheet of thickness $d$ is modelled as two semi-infinite elastic plates separated at $x = 0$ due to an open crack and floating on an undisturbed water surface $y = 0$, $-\infty < x < \infty$. Further, the fluid and ice characteristics remain the same, as discussed in § 2. In the present context, we will pose the physical problem in terms of the spatial velocity potential after eliminating the spatial surface elevation $\eta(x)$ from various boundary conditions. Under the above assumptions, the spatial velocity potential satisfies Laplace equation in the fluid domain (2.1) along with the ice-covered boundary condition (2.2) and the bottom conditions (2.3).

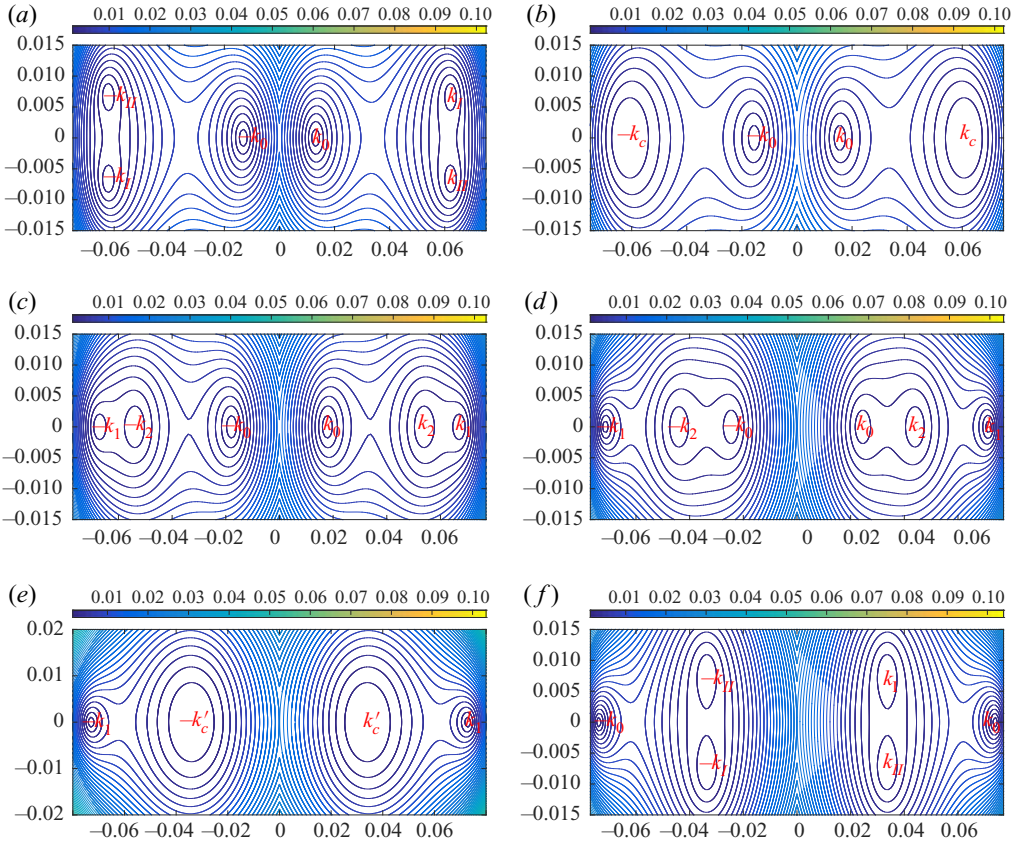


Figure 3. Contour plots of dispersion relation for different values of incoming wave frequencies are shown. The location of the roots are shown with the small circles which moves in the complex plane with changing frequency. (*a*) For one real root ($\omega = 0.345$ s$^{-1}$), (*b*) during secondary blocking ($\omega = 0.3696$ s$^{-1}$), (*c*) for three real roots ($\omega = 0.39$ s$^{-1}$), (*d*) for three real roots ($\omega = 0.43$ s$^{-1}$), (*e*) during primary blocking ($\omega = 0.4512$ s$^{-1}$), (*f*) for one real root ($\omega = 0.465$ s$^{-1}$) when compressive stress $Q = 1.75\sqrt{D}$. (*a*) Prior to secondary blocking. (*b*) Secondary blocking point. (*c*) Generation of three positive and negative real roots. (*d*) Movement of the middle root. (*e*) Primary blocking point. (*f*) Root after primary blocking.

Moreover, across the interface boundary between the two plate-covered regions, the continuity of velocity and pressure yields

$$\phi_x(0+, y) = \phi_x(0-, y) \quad \text{and} \quad \phi(0+, y) = \phi(0-, y) \quad \text{in } 0 < y < \infty. \tag{3.1}$$

Further, assuming the free-edge conditions (zero bending moment and shear stress) are complied with near the crack (as in Sahoo 2012), the velocity potential $\phi(x, y)$ will satisfy the following relations:

$$B\{\phi(x, y)\} \equiv D\left[\frac{\partial^2}{\partial x^2}\left(\frac{\partial \phi}{\partial y}\right)\right]_{y=0} \to 0 \quad \text{as } x \to 0\pm, \tag{3.2}$$

and

$$S\{\phi(x, y)\} \equiv \left[D\frac{\partial^3}{\partial x^3}\left(\frac{\partial \phi}{\partial y}\right) + Q\frac{\partial^2 \phi}{\partial x \partial y}\right]_{y=0} \to 0 \quad \text{as } x \to 0\pm. \tag{3.3}$$

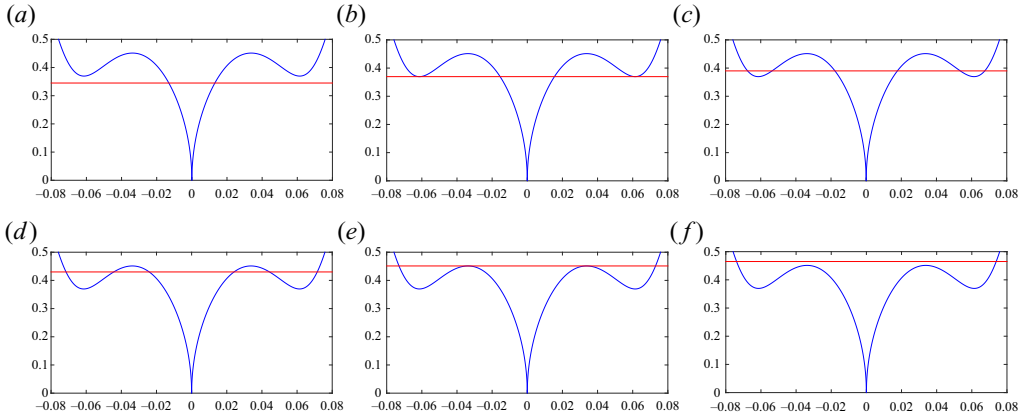


Figure 4. Dispersion graphs for the same set of data values taken in figure 3. (*a*) Prior to secondary blocking. (*b*) Secondary blocking point. (*c*) Generation of three positive and negative real roots. (*d*) Movement of the middle root. (*e*) Primary blocking point. (*f*) Root after primary blocking.

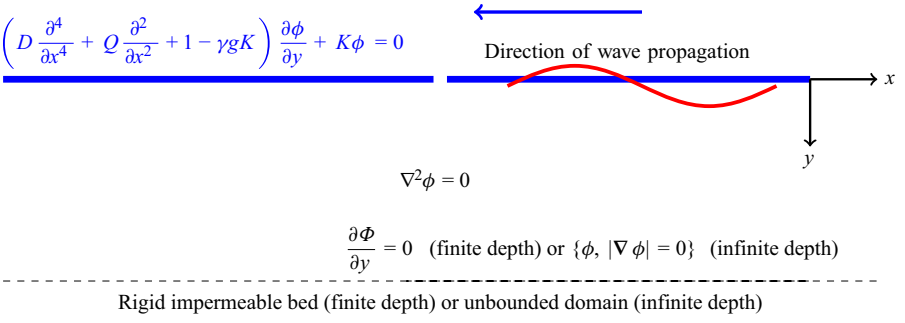


Figure 5. Schematic diagram of a floating ice sheet having a crack.

The choice of free-edge conditions is made primarily because this is the most straightforward and standard boundary condition. It could be argued that under compression, other energy-conserving boundary conditions may be more appropriate (Lee & Newman 2000; Xia, Kim & Ertekin 2000; Karmakar & Sahoo 2005; Kohout & Meylan 2009). Such boundary conditions could be incorporated without any modification to the current method, but we do not do so here like this for simplicity. Finally, the velocity potential satisfies Sommerfeld's radiation boundary condition, which for one travelling wavenumber is given by

$$\phi(x, y) = \begin{cases} \dfrac{\mathrm{i}g}{\omega}\left(\mathrm{e}^{-\mathrm{i}k_0 x} + R_0\,\mathrm{e}^{\mathrm{i}k_0 x}\right) f_0(y) & \text{as } x \to \infty, \\ \dfrac{\mathrm{i}g}{\omega} T_0\,\mathrm{e}^{-\mathrm{i}k_0 x} f_0(y) & \text{as } x \to -\infty, \end{cases} \tag{3.4}$$

with $k_0$ being a real root of the dispersion relations (2.7) with $R_0$ and $T_0$ being the complex constants associated with the amplitudes of the reflected and transmitted waves, respectively. However, in a system having multiple propagating modes, the above forms

modify into

$$\phi(x,y)=\begin{cases}\dfrac{\mathrm{i}g}{\omega}\left\{\left(\mathrm{e}^{-\mathrm{i}\epsilon_0 k_0 x}+R_0\,\mathrm{e}^{\mathrm{i}\epsilon_0 k_0 x}\right)f_0(y)+\displaystyle\sum_{i=1}^{p}R_i\,\mathrm{e}^{\mathrm{i}\epsilon_i k_i x}f_i(y)\right\} & \text{as } x\to\infty,\\ \dfrac{\mathrm{i}g}{\omega}\displaystyle\sum_{i=0}^{p}T_i\,\mathrm{e}^{-\mathrm{i}\epsilon_i k_i x}f_i(y) & \text{as } x\to-\infty,\end{cases}\tag{3.5}$$

where $k_i$, $(i=0,1,\ldots,p)$ represents $(p+1)$ propagating modes which individually satisfy the radiation condition mentioned in (2.6), $R_i$ and $T_i$ are the complex constants associated with the amplitude of the reflected and transmitted waves in the $i$th mode and $\epsilon_i=\pm1$ when $\mathrm{d}\omega/\mathrm{d}k|_{k=k_i}\gtrless 0$.

## 4. Method of solution

Exploiting the geometrical symmetry of the physical problem about $x=0$, the BVP defined in the half-plane in the previous section is reduced to two quarter plane BVPs (following the reduction approach adopted in Manam *et al.* 2005) whose solutions are sought based on the mixed type of Fourier transform as discussed in § 2. The reduced potentials are defined as

$$\varphi(x,y)=\phi(x,y)-\phi(-x,y)\quad\text{and}\quad\Upsilon(x,y)=\phi(x,y)+\phi(-x,y),\quad x>0.\tag{4.1}$$

Thus, $\varphi(x,y)$ and $\Upsilon(x,y)$ satisfy the governing equation (2.1) in the quarter plane $x>0$, $y>0$ along with the plate-covered condition (2.2) and the bottom condition (2.3) independently. Finally, the continuity conditions in (3.1) yields

$$\Upsilon_x(x,y)=0\quad\text{and}\quad\varphi(x,y)=0\quad\text{at } x=0,\,0<y<\infty.\tag{4.2}$$

From the continuity equation (4.2), it is clear that $\varphi(x,y)$ satisfies (2.4) and $\Upsilon(x,y)$ satisfies (2.5) with $\varphi(0,y)=u(y)=0$ and $\Upsilon_x(0,y)=v(y)=0$ for $0<y<\infty$. The edge conditions (3.2) and (3.3) for the bending moment and shear force in terms of $\varphi(x,y)$ and $\Upsilon(x,y)$ yield

$$D\frac{\partial^2}{\partial x^2}\left(\frac{\partial\Upsilon(0,0)}{\partial y}\right)=0,\quad D\frac{\partial^3}{\partial x^3}\left(\frac{\partial\Upsilon(0,0)}{\partial y}\right)+Q\frac{\partial^2\Upsilon(0,0)}{\partial x\partial y}=0,\tag{4.3a,b}$$

$$D\frac{\partial^2}{\partial x^2}\left(\frac{\partial\varphi(0,0)}{\partial y}\right)=0,\quad D\frac{\partial^3}{\partial x^3}\left(\frac{\partial\varphi(0,0)}{\partial y}\right)+Q\frac{\partial^2\varphi(0,0)}{\partial x\partial y}=0.\tag{4.4a,b}$$

The expansion formulae for distinct roots of the dispersion relation derived in § 2 will be applied here to derive the expression for reduced potentials in both cases of infinite and finite depth water domain.

### 4.1. *Infinite depth water domain*

Here, the reduced potential $\varphi(x,y)$ is expanded as

$$\varphi(x,y)=\frac{\mathrm{i}g}{\omega}\left[\mathrm{e}^{-\mathrm{i}k_0x-k_0y}+A_0f_0(y)\,\mathrm{e}^{\mathrm{i}k_0x}+A_If_I(y)\,\mathrm{e}^{\mathrm{i}k_Ix}+A_{II}f_{II}(y)\,\mathrm{e}^{-\mathrm{i}k_{II}x}+\frac{2}{\pi}\int_0^\infty\frac{A(\xi)M(\xi,y)\,\mathrm{e}^{-\xi x}\,\mathrm{d}\xi}{\Delta(\xi)}\right],\tag{4.5}$$

where $\Delta(\xi)$, $M(\xi, y)$ and the eigenfunctions $f_n(y)(n = 0, I, II)$ for infinite depth are the same as defined in § 2. In between the frequency band of primary and secondary blocking, when three propagating modes exist, we denote the positive real roots as $k_0$, $k_1$ and $k_2$ where $k_2$ is the root corresponding to negative energy flux. The form of the reduced potential given by (4.5) is valid with $k_I$, $k_{II}$ replaced by $k_1$, $k_2$, respectively, and even at the time of blocking in which case either $k_1 = k_2$ or $k_0 = k_2$. Without loss of generality, we solve the problem with the case of complex roots $k_I$, $k_{II}$, and easily extend it to the multiple real roots $k_1$, $k_2$.

Utilizing the relation (4.2) along with the edge boundary conditions (4.4*a*,*b*) and the orthogonal property of the eigenfunctions as in (2.13) and (2.15), the unknown coefficients, $A_n$ and $A(\xi)$, are obtained as

$$\left.\begin{gathered} A_0 = \frac{\omega}{\mathrm{i}g}\frac{k_0}{KC_0}\left(Q - Dk_0^2\right)\alpha_1 - 1, \quad A_I = \frac{\omega}{\mathrm{i}g}\frac{k_I}{KC_I}\left(Q - Dk_I^2\right)\alpha_1, \\ A(\xi) = \frac{\omega}{\mathrm{i}g}\xi\left(Q + D\xi^2\right)\alpha_1, \quad A_{II} = \frac{\omega}{\mathrm{i}g}\frac{k_{II}}{KC_{II}}\left(Q - Dk_{II}^2\right)\alpha_1, \quad \alpha_1 = \frac{2\mathrm{i}k_0^2\left(Q - Dk_0^2\right)}{\beta_1}, \\ \beta_1 = \frac{\omega}{\mathrm{i}g}\left\{\frac{\mathrm{i}k_0^3}{KC_0}(Q - Dk_0^2)^2 + \frac{\mathrm{i}k_I^3}{KC_I}\left(Q - Dk_I^2\right)^2 - \frac{\mathrm{i}k_{II}^3}{KC_{II}}\left(Q - Dk_{II}^2\right)^2\right. \\ \left. - \frac{2K}{\pi}\int_0^\infty \frac{\xi^3\left(Q + D\xi^2\right)^2\,\mathrm{d}\xi}{\Delta(\xi)}\right\}. \end{gathered}\right\} \tag{4.6}$$

Proceeding in a similar manner, the reduced potential $\Upsilon(x, y)$ is expressed as

$$\Upsilon(x, y) = \frac{\mathrm{i}g}{\omega}\left[\mathrm{e}^{-\mathrm{i}k_0x - k_0y} + B_0 f_0(y)\,\mathrm{e}^{\mathrm{i}k_0x} + B_I f_I(y)\,\mathrm{e}^{\mathrm{i}k_Ix} + B_{II} f_{II}(y)\,\mathrm{e}^{-\mathrm{i}k_{II}x} + \frac{2}{\pi}\int_0^\infty \frac{B(\xi)M(\xi, y)\,\mathrm{e}^{-\xi x}\,\mathrm{d}\xi}{\Delta(\xi)}\right]. \tag{4.7}$$

The unknown constants $B_n$, for $n = 0, I, II$. and the unknown function $B(\xi)$ being

$$\left.\begin{gathered} B_0 = \frac{\omega}{g}\frac{Dk_0^2}{KC_0}\alpha_2 + 1, \quad B_I = \frac{\omega}{g}\frac{Dk_I^2}{KC_I}\alpha_2, \quad B(\xi) = -\frac{\omega}{\mathrm{i}g}D\xi^2\alpha_2, \quad B_{II} = -\frac{\omega}{g}\frac{Dk_{II}^2}{KC_{II}}\alpha_2, \\ \alpha_2 = \frac{-2k_0^3}{\beta_2}, \quad \beta_2 = \frac{\omega}{\mathrm{i}g}\left\{\frac{\mathrm{i}Dk_0^5}{KC_0} + \frac{\mathrm{i}Dk_I^5}{KC_I} - \frac{\mathrm{i}Dk_{II}^5}{KC_{II}} + \frac{2K}{\pi}\int_0^\infty \frac{D\xi^5\,\mathrm{d}\xi}{\Delta(\xi)}\right\}. \end{gathered}\right\} \tag{4.8}$$

Within the frequency band of primary and secondary blocking, $k_I$ and $k_{II}$ become real valued, redefined as $k_1$ and $k_2$, respectively, with the relation $k_0 < k_2 < k_1$, and the same potential form obtained in (4.5) is valid. In the subsequent sections, all the analysis and results are shown for the case of infinite depth water domain only. However, it is deemed suitable to provide the form of the potential functions for finite depth water domain.

### 4.2. *Finite depth water domain*

The reduced potential $\varphi(x, y)$ in this case can be expressed as

$$\varphi(x,y) = \frac{\mathrm{i}g}{\omega}\left[\left(\mathrm{e}^{-\mathrm{i}k_0x} + A_0\,\mathrm{e}^{\mathrm{i}k_0x}\right) f_0(y) + A_I\,\mathrm{e}^{\mathrm{i}k_Ix} f_I(y) + A_{II}\,\mathrm{e}^{-\mathrm{i}k_{II}x} f_{II}(y) + \sum_{n=1}^{\infty} A_n f_n(y)\,\mathrm{e}^{-k_nx}\right], \tag{4.9}$$

where the eigenfunctions $f_n(y)$ $(n = 0, I, II, 1, 2, 3\ldots.)$ for finite depth are the same as defined in § 2.

Using (4.2), (4.4*a*,*b*) and (2.20), the unknown coefficients, $A_n$, are obtained as

$$\left.\begin{aligned} A_0 &= \frac{\omega}{\mathrm{i}g}\frac{k_0\tanh k_0h}{KC_0}\left(Q - Dk_0^2\right)\alpha_1 - 1,\\ A_n &= \frac{\omega}{\mathrm{i}g}\frac{k_n\tanh k_nh}{KC_n}\left(Q - Dk_n^2\right)\alpha_1, \quad \text{for } n = I, II, 1, 2, 3, \ldots,\\ \alpha_1 &= \frac{2\mathrm{i}k_0^2\tanh(k_0h)\left(Q - Dk_0^2\right)}{\beta_1}, \quad \text{and} \quad k_n = \mathrm{i}k_n \quad \text{for } n = 1, 2, 3, \ldots,\\ \beta_1 &= \frac{\omega}{\mathrm{i}g}\left[\frac{\mathrm{i}k_0^3\tanh^2(k_0h)}{KC_0}(Q - Dk_0^2)^2 + \frac{\mathrm{i}k_I^3\tanh^2(k_Ih)}{KC_I}\left(Q - Dk_I^2\right)^2\right.\\ &\quad \left. - \frac{\mathrm{i}k_{II}^3\tanh^2(k_{II}h)}{KC_{II}}\left(Q - Dk_{II}^2\right)^2 - \sum_{n=1}^{\infty}\frac{k_n^3}{KC_n}\left\{\left(Q + Dk_n^2\right)\tan(k_nh)\right\}^2\right]. \end{aligned}\right\} \tag{4.10}$$

Likewise, the reduced potential $\Upsilon(x, y)$ is expressed as

$$\Upsilon(x,y) = \frac{\mathrm{i}g}{\omega}\left[\left(\mathrm{e}^{-\mathrm{i}k_0x} + B_0\,\mathrm{e}^{\mathrm{i}k_0x}\right) f_0(y) + B_I\,\mathrm{e}^{\mathrm{i}k_Ix} f_I(y) + B_{II}\,\mathrm{e}^{-\mathrm{i}k_{II}x} f_{II}(y) + \sum_{n=1}^{\infty} B_n f_n(y)\,\mathrm{e}^{-k_nx}\right], \tag{4.11}$$

with the unknown constants, $B_n$, obtained as

$$\left.\begin{aligned} B_0 &= \frac{\omega}{g}\frac{Dk_0^2\tanh k_0h}{KC_0}\alpha_2 + 1, \quad B_n = \frac{\omega}{g}\frac{Dk_n^2\tanh k_nh}{KC_n}\alpha_2, \quad \text{for } n = I, 1, 2, 3, \ldots\\ B_{II} &= -\frac{\omega}{g}\frac{Dk_{II}^2\tanh k_{II}h}{KC_{II}}\alpha_2, \quad \alpha_2 = -\frac{2k_0^3\tanh(k_0h)}{\beta_2},\\ \beta_2 &= \frac{\omega}{\mathrm{i}g}\left\{\frac{\mathrm{i}k_0^5D\tanh^2(k_0h)}{KC_0} + \frac{\mathrm{i}k_I^5D\tanh^2(k_Ih)}{KC_I} - \frac{\mathrm{i}k_{II}^5D\tanh^2(k_{II}h)}{KC_{II}}\right.\\ &\quad \left. + \sum_{n=1}^{\infty}\frac{Dk_n^5\tan^2(k_nh)}{KC_n}\right\}. \end{aligned}\right\} \tag{4.12}$$

Next, we shift our focus to the case of infinite water depth in the subsequent analysis. While extending the result from complex roots $k_I$, $k_{II}$ to real roots $k_1$, $k_2$, all the notations used will also be redefined by replacing the suffices $I$, $II$ with 1, 2, respectively. Since there are three progressive wave modes present in the system, each of which travels with different group velocity, the reflection and transmission coefficients which express the transport of energy must be derived with care.

## 5. Energy balance relation

In the theoretical study of scattering of water waves, the energy balance relation or energy identity plays a pivotal role in the understanding of scattering of wave energy and exhibits the relation among the scattering coefficients such as the reflection and transmission coefficients. Often, the energy identity is used as a check of the computed results of these scattering coefficients. In this section, the energy identity is derived using Green's integral theorem involving the complex velocity potential and its complex conjugate. Further, the occurrence of negative group velocity in the system will be demonstrated with the derived energy identity.

To obtain the energy identity, we use Green's integral theorem, as given by

$$\int_C \left(\bar{\phi}\frac{\partial \phi}{\partial n} - \phi\frac{\partial \bar{\phi}}{\partial n}\right) \mathrm{d}s = 0, \tag{5.1}$$

where $C$ denotes the closed boundary of the fluid region, which is union of two closed boundary $C_1$ and $C_2$, $\bar{\phi}$ is the complex conjugate of $\phi$, which satisfies (2.1)–(2.3) and (3.1)–(3.5), and $\partial/\partial n$ represents the outward normal derivative to the closed boundary $C$. The closed boundary $C_1$ consists of the horizontal upper surface ($0 < x < X$; $y = 0$), vertical boundaries ($0 < y < \infty$; $x = X$), bottom boundary ($0 < x < X$; $y \to \infty$) and vertical boundary at the crack ($0 < y < \infty$; $x = 0$), and closed boundary $C_2$ consists of the horizontal upper surface ($-X < x < 0$; $y = 0$), vertical boundaries ($0 < y < \infty$; $x = -X$), bottom boundary ($-X < x < 0$; $y \to \infty$) and vertical boundary at the crack ($0 < y < \infty$; $x = 0$), ultimately letting $X \to \infty$.

Using the boundary conditions and the far-field radiation condition in (5.1), we obtain the energy relation as given by

$$K_r^2 + K_t^2 = 1, \tag{5.2}$$

where

$$\left.\begin{aligned} K_r^2 &= \left|\frac{B_0 + A_0}{2}\right|^2 + \left(\frac{k_1 C_g(k_1)}{k_0 C_g(k_0)}\right)\left|\frac{B_1 + A_1}{2}\right|^2 - \left(\frac{k_2 C_g(k_2)}{k_0 C_g(k_0)}\right)\left|\frac{B_2 + A_2}{2}\right|^2, \\ K_t^2 &= \left|\frac{B_0 - A_0}{2}\right|^2 + \left(\frac{k_1 C_g(k_1)}{k_0 C_g(k_0)}\right)\left|\frac{B_1 - A_1}{2}\right|^2 - \left(\frac{k_2 C_g(k_2)}{k_0 C_g(k_0)}\right)\left|\frac{B_2 - A_2}{2}\right|^2 \end{aligned}\right\} \tag{5.3}$$

and

$$C_g(k_j) = \frac{1}{2}\sqrt{\frac{g}{k_j}}\frac{(5Dk_j^4 - 3Qk_j^2 + 1) + 2k_j^3 g\gamma(2Dk_j^2 - Q)}{(1 + k_j g\gamma)\sqrt{(1 + k_j g\gamma)(Dk_j^4 - Qk_j^2 + 1)}} \quad \text{for } j = 0, 1, 2, \tag{5.4}$$

with $k_0$ being the wavenumber associated with the incident wave.

The newly defined reflection ($K_r$) and transmission ($K_t$) coefficients are now plotted against $T = 2\pi/\omega$ in figure 6 for three values of compressive stress. It is observed that

both the coefficients now have values less than one within the frequency band of primary and secondary blocking in which the dispersion relation possesses three distinct real roots (see figure 6*b*). Moreover, the transitions of $K_r$ and $K_t$ at the primary and secondary blocking points are also shown in figures 6(*a*) and 6(*c*), respectively, for the same values of compressive stress. A continuous transition is observed and this validates the correctness of the newly derived expressions for $K_r$ and $K_t$. We here mention that, in order to compute $K_r$ and $K_t$ outside the frequency band of primary and secondary blocking, the following formulae have been used due to the existence of only one propagating mode:

$$K_r^2 = \left|\frac{B_0 + A_0}{2}\right|^2 \quad \text{and} \quad K_t^2 = \left|\frac{B_0 - A_0}{2}\right|^2. \tag{5.5a,b}$$

A similar study for three different values of plate thickness is carried out, and the results are graphically shown in figure 7. Similar observations as were made in figure 6 are made in this case as well. The only difference is observed in terms of the values of $T$ at which the primary and secondary blocking points are obtained. Corresponding primary and secondary blocking occur at higher values of $T$ as the plate thickness increases.

## 6. Scattering process through the primary and secondary blocking points

In this section, we will discuss the scattering process due to a crack when primary and secondary blocking occur under the influence of fixed compressive stress acting on the plate. Without loss of generality, we can consider the case of secondary blocking in which any incoming frequency lower than the blocking frequency corresponds to one propagating mode, and any higher frequency generates three propagating modes. A similar process happens in the case of the primary blocking, with the only difference being the occurrence of three propagating modes at a frequency lower than that of the blocking frequency. The transition from one propagating mode to three or *vice versa* occurs through the blocking frequency. It is thus intuitive to say that this transition occurs continuously, and the justification follows below.

At the instance of secondary blocking, one can have $\pm k_I = \pm k_1 = \pm k_{II} = \pm k_2 = \pm k_c$ (see figure 8). However, the potential form (4.5) is still valid since $k_1$, and $-k_2$ are two different values, albeit their absolute values being the same. The potential form given by (4.5) reflects the fact that the root $k_2$, corresponding to the waves with negative energy flux, is taken from the negative wavenumber region (of the form $-k_2$). The movement of the roots of the dispersion relation in the complex plane plays a pivotal role in the scattering process through the blocking frequency. Four complex roots $\pm k_I$ and $\pm k_{II}$, and two real roots $\pm k_0$ of the dispersion relation are the possible choices of wave modes for the physical process, to begin with. Next, we look for those roots which provide a bounded solution for the scattering problem due to the crack. Hence, the roots of the form $k_0$, $k_I$, $-k_{II}$ are the suitable candidates to provide bounded solution in the region $x > 0$. Consequently, even though $k_I$ merges with $k_{II}$ at the moment of secondary blocking, it is feasible to continue the process with $-k_{II}$. An equivalent choice of roots in the region $x < 0$ will be $-k_0$, $-k_I$, $k_{II}$, and similarly the process may continue with $k_{II}$ when $-k_I$ merges with $-k_{II}$. In this sense, the root $-k_{II}$ is qualitatively equivalent to the root $k_{II}$ for the crack problem. As soon as the complex roots $k_I$ and $k_{II}$ merge at $k_c$, they can take the form $k_1$ and $k_2$, respectively. The same goes for their counterpart on the left side half. Following the earlier discussion of figure 3, although $k_I$, $k_{II}$ merges at $k_c$, the contribution from $k_{II}$ (equivalently $k_2$) can be obtained from $-k_{II}$ (equivalently $-k_2$). Consequently, the overlapping of the roots at the blocking points can be avoided simply by taking one root from the negative real axis.

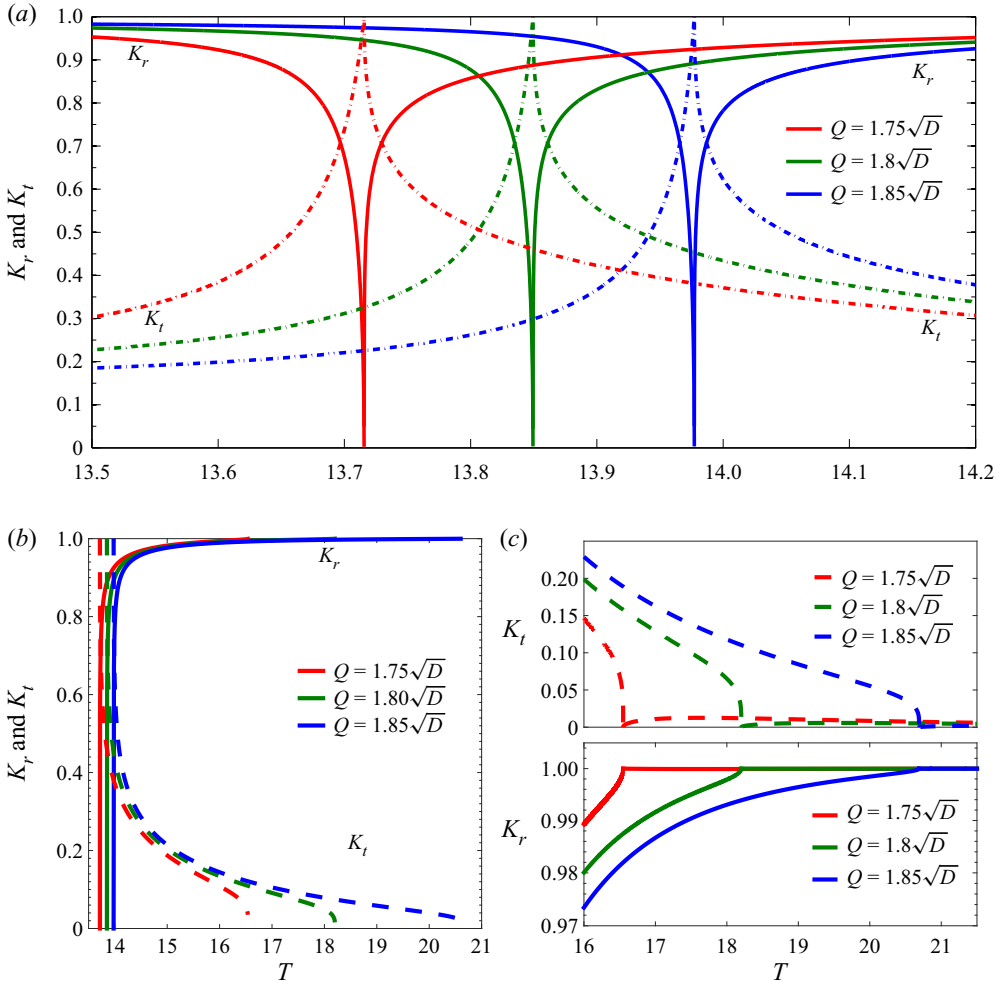


Figure 6. Values of $K_r$ and $K_t$ are plotted for three different values of compressive stress. Panel (*a*) depicts the continuity of $K_r$ and $K_t$ across primary blocking frequency. Sharp corners in the graphs are due to the blocking; $k_I$ is the incident wave after primary blocking. Panel (*b*) depicts $K_r$ and $K_t$ within the frequency band of primary and secondary blocking in which three propagating modes exist. Both the coefficient values are below one after using the modified energy relation. Panel (*c*) depicts the continuity of $K_r$ and $K_t$ across secondary blocking frequency; $k_0$ is the incident wave before secondary blocking. (*a*) Transition through primary blocking. (*b*) Within the frequency band of primary and secondary blocking. (*c*) Transition through secondary blocking.

Thus, the theory for distinct roots is unequivocally applicable at the secondary blocking. A similar situation arises at the time of primary blocking where $\pm k_I = \pm k_0 = \pm k_{II} = \pm k_2 = \pm k_c'$. An exactly similar process but of reverse order will happen that will bifurcate $\pm k_c'$ into the complex plane to regenerate the roots $\pm k_I$, $\pm k_{II}$. The locus of the roots of the dispersion relation during the complete scattering process is depicted for three different values of compressive stress. The scattering process through the blocking frequency is thus smooth due to the continuous movement of the roots of the dispersion relation in the complex plane without any kind of overlapping.

It is, however, feasible to consider any of the three propagating modes (in the frequency band of primary and secondary blocking) as the incident wave and hence the potential

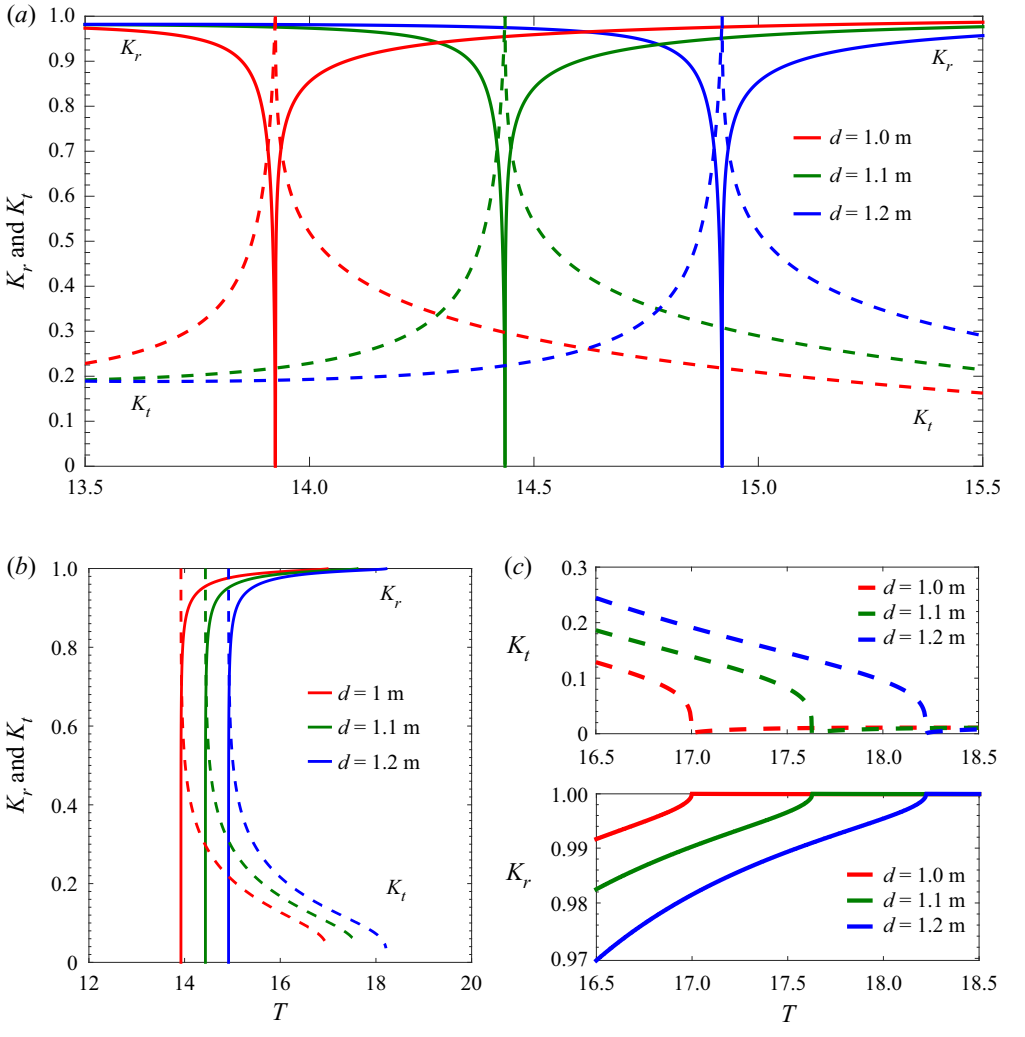


Figure 7. Values of $K_r$ and $K_t$ are plotted for three different values of plate thickness. (*a*) Transition through primary blocking. (*b*) Within the frequency band of primary and secondary blocking. (*c*) Transition through secondary blocking.

function can be written as

$$\begin{pmatrix}\phi_{1r}(x,y)\\ \phi_{2r}(x,y)\\ \phi_{3r}(x,y)\end{pmatrix} = \frac{\mathrm{i}g}{\omega}\left[\begin{pmatrix}I_{00} & 0 & 0\\ 0 & I_{01} & 0\\ 0 & 0 & I_{02}\end{pmatrix}\begin{pmatrix}\mathrm{e}^{-\mathrm{i}k_0 x}f_0(y)\\ \mathrm{e}^{-\mathrm{i}k_1 x}f_1(y)\\ \mathrm{e}^{\mathrm{i}k_2 x}f_2(y)\end{pmatrix} + \overbrace{\begin{pmatrix}K_{r11} & K_{r12} & K_{r13}\\ K_{r21} & K_{r22} & K_{r23}\\ K_{r31} & K_{r32} & K_{r33}\end{pmatrix}}^{\text{Scattering matrix } (S_R)}\begin{pmatrix}\mathrm{e}^{\mathrm{i}k_0 x}f_0(y)\\ \mathrm{e}^{\mathrm{i}k_1 x}f_1(y)\\ \mathrm{e}^{-\mathrm{i}k_2 x}f_2(y)\end{pmatrix} + \frac{2}{\pi}\begin{pmatrix}a\\ a\\ a\end{pmatrix}\right] \quad \text{for } x > 0, \quad (6.1)$$

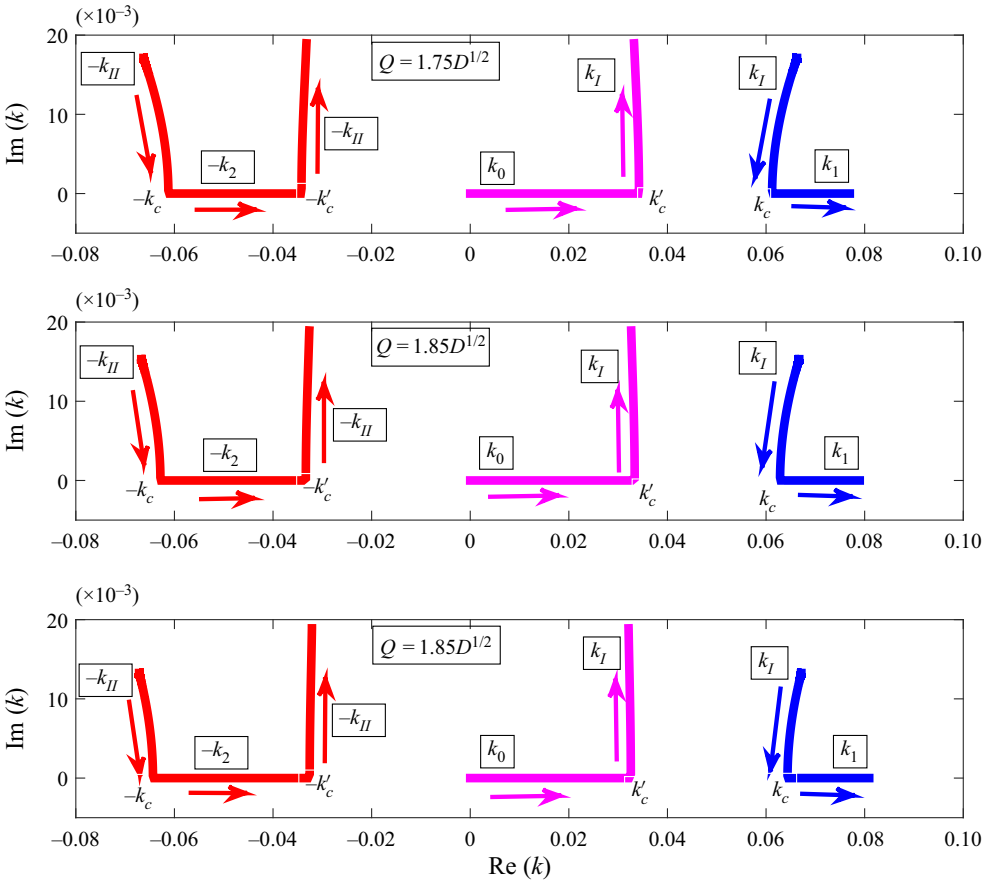


Figure 8. The movement of roots of the dispersion relation with an increase in frequency is shown for different values of compressive stress $Q$. For each of the figures, the first point of simultaneous contact in the real axis for red and blue curves (roots which are travelling from the complex plane) corresponds to secondary blocking. With further increase in frequency, the roots move along the real axis in the direction as shown in the figure. Then, at the primary blocking, the red and pink curve simultaneously leave the real axis to move in the complex plane. All the three roots are distinct during the scattering process, even during blocking, unlike in the case of plane wave propagation in which root coalescence occurs. Consequently, the theory of distinct roots of the dispersion relation will work perfectly in the scattering process.

with

$$a = \int_0^\infty \frac{A(\xi)M(\xi, y)\,\mathrm{e}^{-\xi x}\,\mathrm{d}\xi}{\Delta(\xi)}, \tag{6.2}$$

and $\phi_{jr}$ $(j = 1, 2, 3)$ represents the form of the velocity potential when $k_i$ $(i = 0, 1, 2)$ is the incident wave mode, respectively. The scattering matrix, denoted by $S_R$, defines the relationship between the forward and backward moving waves ($k_0 < k_2 < k_1$). It is to be noted that the direction of the wave envelope for $k_2$ is opposite to that of $k_0$ and $k_1$. The $j$th row $(j = 1, 2, 3)$ of it respectively corresponds to $k_i$ as the incident wave mode $(i = 0, 1, 2)$, and the corresponding amplitude ratios of the reflected waves are $K_{rjl}/I_{0i}$ $(j,\ l = i + 1$ with $i = 0, 1, 2)$ for each $i$, where $I_{0i}$ is the incident wave amplitude of the mode $k_i$ (taken to be unity in the numerical calculation). Moreover, the transmitted velocity

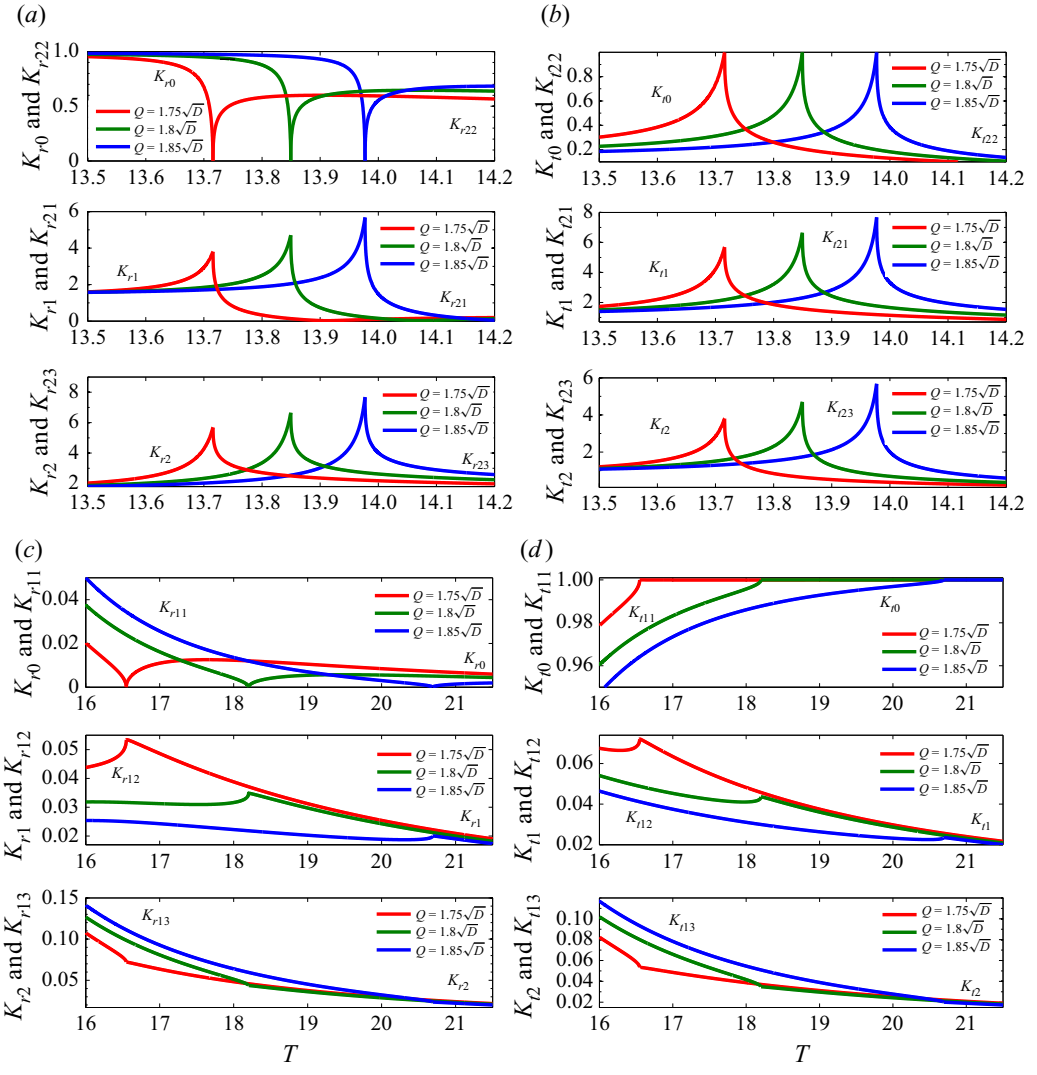


Figure 9. Amplitude ratio of different reflected and transmitted waves are plotted with time period $T$ around the primary and secondary blockings for various values of compressive stress. At secondary blocking, the curve is continuous if $k_0$ is taken as incident wave, whereas $k_I$ becomes the incident wavenumber at the primary blocking. The continuity of the graphs confirms the transformation of wave modes across blocking frequencies as claimed in the figure 8. (*a*) Reflected modes near primary blocking. (*b*) Transmitted modes near primary blocking. (*c*) Reflected modes near secondary blocking. (*d*) Transmitted modes near secondary blocking.

potential can be written as

$$\begin{pmatrix}\phi_{1t}(x,y)\\ \phi_{2t}(x,y)\\ \phi_{3t}(x,y)\end{pmatrix} = \frac{\mathrm{i}g}{\omega}\overbrace{\begin{pmatrix}K_{t11} & K_{t12} & K_{t13}\\ K_{t21} & K_{t22} & K_{t23}\\ K_{t31} & K_{t32} & K_{t33}\end{pmatrix}}^{\text{Scattering matrix } (S_T)}\begin{pmatrix}\mathrm{e}^{-\mathrm{i}k_0 x}f_0(y)\\ \mathrm{e}^{-\mathrm{i}k_1 x}f_1(y)\\ \mathrm{e}^{\mathrm{i}k_2 x}f_2(y)\end{pmatrix} + \frac{2\mathrm{i}g}{\pi\omega}\begin{pmatrix}b\\ b\\ b\end{pmatrix} \quad \text{for } x<0, \quad (6.3)$$

where

$$b = \int_0^\infty \frac{A(\xi)M(\xi, y)\, \mathrm{e}^{\xi x}\, \mathrm{d}\xi}{\Delta(\xi)}, \tag{6.4}$$

and $\phi_{jt}$ $(j = 1, 2, 3)$ represents the form of the velocity potential when $k_i$ $(i = 0, 1, 2)$ is the incident wave mode, respectively. Here, the amplitude ratios of the transmitted waves are $K_{tjl}/I_{0i}$ for each $k_i$. The scattering matrix is denoted by $S_T$.

Outside the frequency band of primary and secondary blocking, there exists only one propagating mode, denoted by $p_0$, and it can be any of the $k_i$ values, and two complex modes $k_I$ and $-k_{II}$ for a bounded solution. Now $K_{ri}$ $(i = 0, 1, 2)$, respectively, represent the amplitude ratio of the modes $p_0$, $k_I$ and $-k_{II}$ in the reflected wave region; $K_{ti}$ is the same in the transmitted wave region. This will provide us further insight into mode conversion in terms of continuous transition of the amplitude ratio across blocking frequency. The scattering matrix is plotted against time period $T$ $(2\pi/\omega)$ in figure 9. Figure 9(*a*,*b*) provides the scattering matrices assuming $k_1$ as the incident wave inside the frequency band of primary and secondary blockings. Sharp corners are occurring at the blocking frequencies. The top graph of figure 9(*a*) shows the continuity of $K_{r0}$ and $K_{r22}$. This means the incident wave $k_1$ remains as the only propagating mode above (or below) the primary blocking frequency (or time period). This is consistent with the root movement described earlier in figure 8 (see the blue curve) in which $k_I$ converts into the propagating mode and remains in the real axis. The middle and bottom graphs show the continuity of $(K_{r1}, K_{r21})$ and $(K_{r2}, K_{r23})$, respectively. This justifies the conversions of mode $k_0$ into $k_I$ and $k_2$ into $-k_{II}$ across the blocking frequency. These findings are consistent with figure 8 if we follow the red and pink curves, respectively. A similar pattern (figure 9*b*) of continuity is observed in the transmitted wave region as well. Figure 9(*c*) provides the mode conversion at the secondary blocking frequency when $k_0$ is being treated as the incident wavenumber. All three subplots show the continuity in amplitude ratio across the blocking frequency, namely $K_{r11}$ and $K_{r0}$, justifying the transformation of $k_0$ as the propagating mode; $K_{r12}$ and $K_{r1}$, justifying the transformation of $k_1$ into $k_I$; $K_{r13}$ and $K_{r2}$, justifying the transformation of $k_2$ into $k_{II}$. These observations are also in accordance with figure 8. An exact similar continuity of these modes in the transmitted wave region can be found in figure 9(*d*). Keeping the plate compression fixed, for example, $Q = 1.75\sqrt{D}$, the same effect can be observed (figure 10*a*) when the plate thickness increases. The plate thickness only increases (or decreases) the time period (or frequency) at which the primary blocking occurs (see figure 10*a*,*b*). A similar pattern is observed at the secondary blocking point as well (figure 10*c*,*d*).

## 7. Plate deflection

The plate deflection $(\omega^2\eta(x)/agk_0)$ in the vertical direction is obtained from the following linearized kinematic condition:

$$\frac{\partial H(x, t)}{\partial t} = \frac{\partial \Phi(x, y, t)}{\partial y} \quad \text{on } y = 0, \tag{7.1}$$

where the flexural-gravity wave elevation $H(x, t) = \eta(x)\, \mathrm{e}^{-\mathrm{i}\omega t}$ and $a$ is the initial wave amplitude, which is kept at unity without loss of generality. The above equation yields the

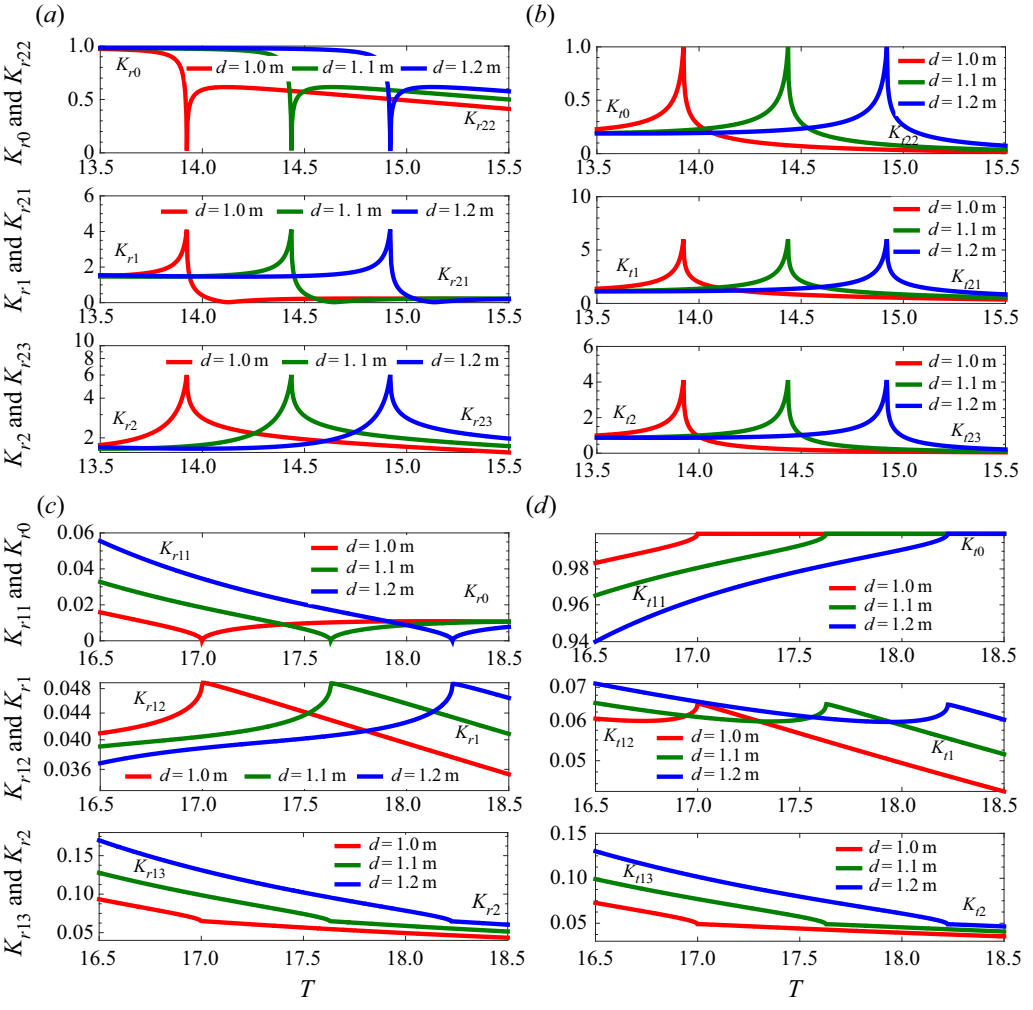


Figure 10. Amplitude ratio of different reflected and transmitted waves are plotted with period $T$ around the primary and secondary blockings for various values of plate thickness for a fixed plate compression $Q = 1.75\sqrt{D}$. It is visible that the period (or frequency) at which both the primary and secondary blockings occur increases (or decreases) with an increase in plate thickness. (*a*) Reflected modes near primary blocking. (*b*) Transmitted modes near primary blocking. (*c*) Reflected modes near secondary blocking. (*d*) Transmitted modes near secondary blocking.

following form of the vertical plate deflection:

$$\frac{\omega^2}{agk_0}\eta(x) = \begin{cases} \dfrac{1}{ak_0}\left[k_0\,\mathrm{e}^{-\mathrm{i}k_0x} + \dfrac{A_0+B_0}{2}k_0\,\mathrm{e}^{\mathrm{i}k_0x} + \dfrac{A_I+B_I}{2}k_I\,\mathrm{e}^{\mathrm{i}k_Ix}\right. \\ \quad \left. + \dfrac{A_{II}+B_{II}}{2}k_{II}\,\mathrm{e}^{-\mathrm{i}k_{II}x} + \dfrac{K}{\pi}\displaystyle\int_0^\infty \dfrac{\{B(\xi)+A(\xi)\}\xi\,\mathrm{e}^{-\xi x}\,\mathrm{d}\xi}{\Delta(\xi)}\right] & \text{for } x > 0, \\ \dfrac{1}{ak_0}\left[\dfrac{B_0-A_0}{2}k_0\,\mathrm{e}^{-\mathrm{i}k_0x} + \dfrac{B_I-A_I}{2}k_I\,\mathrm{e}^{-\mathrm{i}k_Ix}\right. \\ \quad \left. + \dfrac{B_{II}-A_{II}}{2}k_{II}\,\mathrm{e}^{\mathrm{i}k_{II}x} + \dfrac{K}{\pi}\displaystyle\int_0^\infty \dfrac{\{B(\xi)-A(\xi)\}\xi\,\mathrm{e}^{\xi x}\,\mathrm{d}\xi}{\Delta(\xi)}\right] & \text{for } x < 0. \end{cases} \tag{7.2}$$

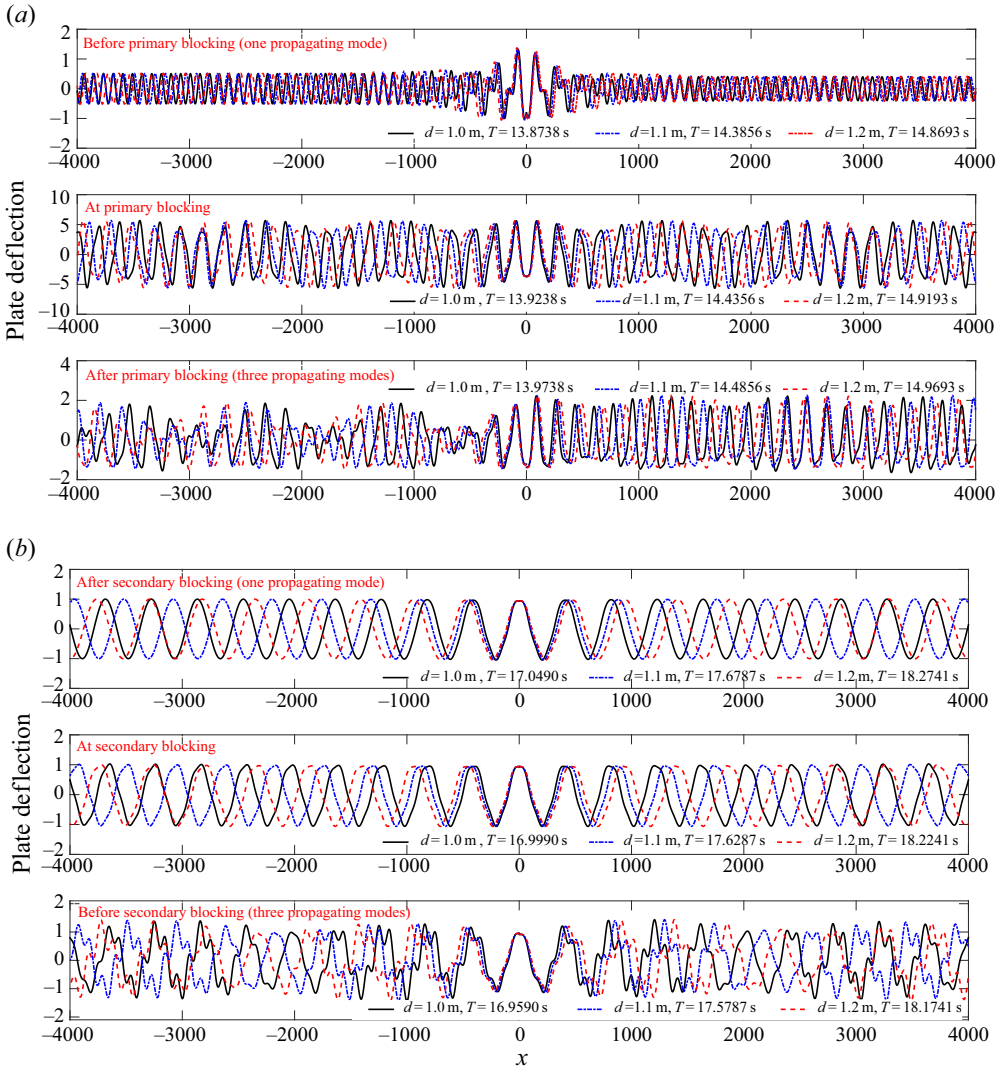


Figure 11. Vertical ice deflection is plotted against spatial distance for different values of ice thickness. Compressive stress $Q = 1.75\sqrt{D}$ is taken for the study. (*a*) Evolution of ice deflection is depicted here at the primary blocking point with upper and lower subplots due to one and multiple propagating modes, respectively. (*b*) The same graph for the secondary blocking point.

The evolution of the plate deflection against spatial distance as the propagating wave modes transit through primary and secondary blocking points is depicted in figure 11 for three different plate thickness values. While figure 11(*a*) deals with the transition through the primary blocking point, the same at the secondary blocking point is illustrated in figure 11(*b*). The top subplot in figure 11(*a*) shows the plate profile just before the primary blocking at which an increase in the amplitude is observed around the crack at $x = 0$. Otherwise, the wave profile is very regular away from the crack. The middle subplot depicts the situation when primary blocking occurs. Since the incident wave gets blocked at the primary blocking point, the wave environment gets very rough. A very high plate amplitude suggests such a concentration of wave energy throughout the plate while

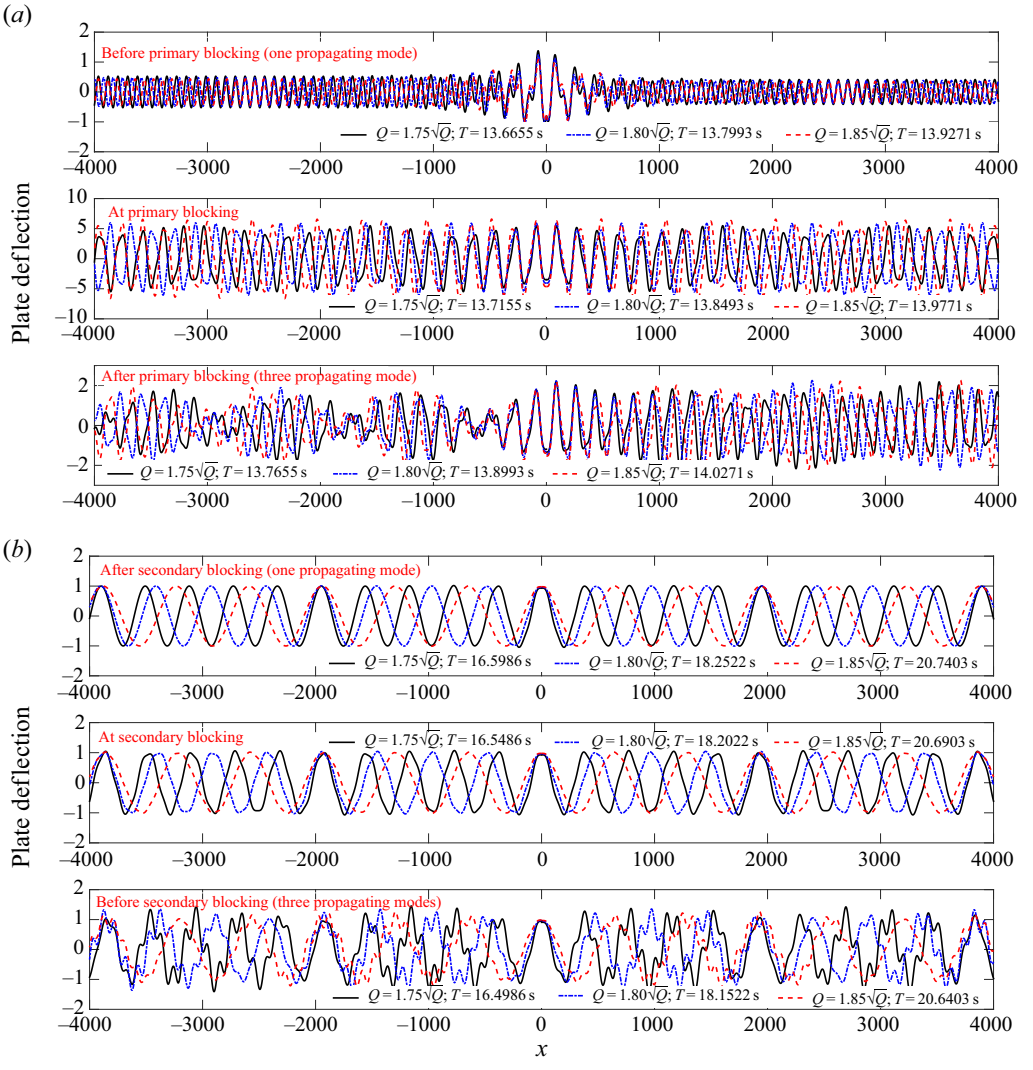


Figure 12. Vertical ice deflection is plotted against spatial distance for different values of compressive stress acting on the ice. Plate thickness is kept fixed as $d = 1$. (*a*) Evolution of ice deflection is depicted here at primary blocking point with upper and lower subplots due to one and multiple propagating modes, respectively. (*b*) The same graph for the secondary blocking point.

the regular pattern of the deflection starts deteriorating. After the primary blocking, the wave with negative energy flux starts propagating and distributes the energy among three wave modes. The superposition of three propagating wave modes makes the wave profile irregular, but the wave amplitude diminishes compared to the case when primary blocking occurs (lower subplot). It is also observed that the deflection is discontinuous in nature near the crack for all three cases (before, after and at blocking frequencies). However, the maximum amplitude is still larger than that of the case of a single propagating mode (from the visual comparison with the top subplot). The effect of the wave with negative energy flux can be seen from the deflection seen in $x < 0$. When the wave packet impinges on the crack, it interacts with the wave profile on the $x > 0$ region and creates a different

wave profile than observed in the $x < 0$ region. A further increase in $T$ (equivalently, decrease in $\omega$) creates the secondary blocking point at which the wave with negative energy flux merges with one of the propagating modes. The nature of the irregularity in the deflection profile becomes very prominent (bottom subplot of figure 11*b*). Since one of the waves responsible for this blocking point has negative energy flux, the ice deflection is not as high (middle subplot) as was observed in the primary blocking point. After the secondary blocking, the only remaining propagating mode has a smaller wavelength and lower frequency compared to the case when one propagating mode was observed before primary blocking. This mode does not have as significant an influence at the crack as was found before primary blocking. The values of $T$ for which the primary and secondary blockings occur increase with an increase in plate thickness, and the corresponding wave profiles get more dispersed (see the red curves corresponding to $d = 1.2$ m). However, the qualitative nature of the profiles remains the same.

Figure 12 illustrates the same study for different values of the compressive stress while keeping the plate thickness fixed. The pattern of the graphs is very similar that discussed for figure 11. Just like the effect of plate thickness discussed earlier, a higher value of compressive stress disperses the wave more.

## 8. Conclusion

Flexural-gravity wave scattering due to a crack is revisited by taking into account the effects of wave blocking. Emphasis is placed on the blocking frequencies for a fixed compression acting on the plate. A continuous transition of amplitudes of different propagating modes is observed at the blocking frequency. An energy identity due to the existence of those propagating modes is established using Green's theorem and later applied in the scattering matrix to identify the incident and transmitted wave modes when the incoming wave frequency varies through the blocking frequencies. It is found that the propagating wave mode with the highest value of wavenumber acts as the incident wave during primary blocking. But, for secondary blocking, the opposite happens, and the wave mode with the lowest wavenumber becomes the incident wave. Movements of the roots of the dispersion relation, or equivalently the different wave modes, are presented in the complex plane. The movement is aligned with the transition of individual wave amplitudes through blocking points and also justifies the choice of the incident and transmitted wave modes. Plate deflection at the primary blocking point is higher compared to that at the secondary blocking point. The regular pattern of the plate deflection is distorted in between due to the propagation of a wave having a negative energy flux.

**Acknowledgements.** This research was supported by the grant number SPARC/2018-2019/P751/SL through the Scheme for Promotion of Academic and Research Collaboration of the Ministry of Human Resource Development, Government of India. M.H.M. acknowledges the support of IIT Kharagpur towards his visit during November–December 2019 during which this work was initiated.

**Declaration of interests.** The authors report no conflict of interest.

**Author ORCIDs.**
S.C. Barman https://orcid.org/0000-0002-2167-7454;
S. Das https://orcid.org/0000-0001-7371-6235;
T. Sahoo https://orcid.org/0000-0003-4234-4568;
M.H. Meylan https://orcid.org/0000-0002-3164-1367.

## References


Abdolali, A., Kadri, U., Parsons, W. & Kirby, J.T. 2018 On the propagation of acoustic-gravity waves under elastic ice sheets. *J. Fluid Mech.* **837**, 640–656.

Barrett, M.D. & Squire, V.A. 1996 Ice-coupled wave propagation across an abrupt change in ice rigidity, density, or thickness. *J. Geophys. Res.: Oceans* **101** (C9), 20825–20832.

Bukatov, A.E. 1980 Influence of a longitudinally compressed elastic plate on the nonstationary wave motion of a homogeneous liquid. *Fluid Dyn.* **15** (5), 687–693.

Bukatov, A.E. & Zav'yalov, D.D. 1995 Impingement of surface waves on the edge of compressed ice. *Fluid Dyn.* **30** (3), 435–440.

Collins, C.O., Rogers, W.E. & Lund, B. 2017 An investigation into the dispersion of ocean surface waves in sea ice. *Ocean Dyn.* **67** (2), 263–280.

Das, S., Kar, P., Sahoo, T. & Meylan, M.H. 2018*a* Flexural-gravity wave motion in the presence of shear current: wave blocking and negative energy waves. *Phys. Fluids* **30** (10), 106606.

Das, S., Sahoo, T. & Meylan, M.H. 2018*b* Dynamics of flexural gravity waves: from sea ice to hawking radiation and analogue gravity. *Proc. R. Soc. Lond.* A **474** (2209), 20170223.

Das, S., Sahoo, T. & Meylan, M.H. 2018*c* Flexural-gravity wave dynamics in two–layer fluid: blocking and dead water analogue. *J. Fluid Mech.* **854**, 121–145.

Davys, J.W., Hosking, R.J. & Sneyd, A.D. 1985 Waves due to a steadily moving source on a floating ice plate. *J. Fluid Mech.* **158**, 269–287.

Evans, D.V. & Porter, R. 2003 Wave scattering by narrow cracks in ice sheets floating on water of finite depth. *J. Fluid Mech.* **484**, 143–165.

Fox, C. & Squire, V.A. 1990 Reflection and transmission characteristics at the edge of shore fast sea ice. *J. Geophys. Res.: Oceans* **95** (C7), 11629–11639.

Fox, C. & Squire, V.A. 1994 On the oblique reflexion and transmission of ocean waves at shore fast sea ice. *Phil. Trans. R. Soc. Lond.* A **347** (1682), 185–218.

Havelock, T.H. 1929 Lix. Forced surface-waves on water. *Lond. Edinb. Dub. Phil. Mag. J. Sci.* **8** (51), 569–576.

Karmakar, D. & Sahoo, T. 2005 Scattering of waves by articulated floating elastic plates in water of infinite depth. *Mar. Struct.* **18** (5–6), 451–471.

Kerr, A.D. 1983 The critical velocities of a load moving on a floating ice plate that is subjected to in-plane forces. *Cold. Reg. Sci. Technol.* **6** (3), 267–274.

Kohout, A.L. & Meylan, M.H. 2009 Wave scattering by multiple floating elastic plates with spring or hinged boundary conditions. *Mar. Struct.* **22** (4), 712–729.

Korobkin, A.A., Malenica, S. & Khabakhpasheva, T. 2018 Interaction of flexural-gravity waves in ice cover with vertical walls. *Phil. Trans. R. Soc. Lond.* A **376** (2129), 20170347.

Kouzov, D.P. 1963 Diffraction of a plane hydro-acoustic wave at a crack in an elastic plate. *Z. Angew. Math. Mech.* **27** (6), 1593–1601.

Lawrie, J.B. 2007 On eigenfunction expansions associated with wave propagation along ducts with wave-bearing boundaries. *IMA J. Appl. Maths* **72** (3), 376–394.

Lawrie, J.B. 2009 Orthogonality relations for fluid-structural waves in a three-dimensional, rectangular duct with flexible walls. *Proc. R. Soc. Lond.* A **465** (2108), 2347–2367.

Lawrie, J.B. & Abrahams, I.D. 1999 An orthogonality relation for a class of problems with high-order boundary conditions; applications in sound-structure interaction. *Q. J. Mech. Appl. Maths* **52** (2), 161–181.

Lee, C.-H. & Newman, J.N. 2000 An assessment of hydroelasticity for very large hinged vessels. *J. Fluids Struct.* **14** (7), 957–970.

Li, Z.F., Wu, G.X. & Ji, C.Y. 2018*a* Interaction of wave with a body submerged below an ice sheet with multiple arbitrarily spaced cracks. *Phys. Fluids* **30** (5), 057107.

Li, Z.F., Wu, G.X. & Ji, C.Y. 2018*b* Wave radiation and diffraction by a circular cylinder submerged below an ice sheet with a crack. *J. Fluid Mech.* **845**, 682–712.

Liu, A.K. & Mollo-Christensen, E. 1988 Wave propagation in a solid ice pack. *J. Phys. Oceanogr.* **18** (11), 1702–1712.

Maïssa, P., Rousseaux, G. & Stepanyants, Y. 2016 Wave blocking phenomenon of surface waves on a shear flow with a constant vorticity. *Phys. Fluids* **28** (3), 032102.

Manam, S.R., Bhattacharjee, J. & Sahoo, T. 2005 Expansion formulae in wave structure interaction problems. *Proc. R. Soc. Lond.* A **462** (2065), 263–287.

Mandal, S., Sahoo, T. & Chakrabarti, A. 2017 Characteristics of eigen-system for flexural gravity wave problems. *Geophys. Astrophys. Fluid Dyn.* **111** (4), 249–281.

Meylan, M. & Squire, V.A. 1994 The response of ice floes to ocean waves. *J. Geophys. Res.: Oceans* **99** (C1), 891–900.

MONDAL, R., MOHANTY, S.K. & SAHOO, T. 2013 Expansion formulae for wave structure interaction problems in three dimensions. *IMA J. Appl. Maths* **78** (2), 181–205.

REN, K., WU, G.X. & LI, Z.F. 2020 Hydroelastic waves propagating in an ice-covered channel. *J. Fluid Mech.* **886**, A18.

RHODES-ROBINSON, P.F. 1971 On the forced surface waves due to a vertical wave-maker in the presence of surface tension. *Math. Proc. Cambridge* **70** (2), 323–337.

RHODES-ROBINSON, P.F. 1979 On surface waves in the presence of immersed vertical boundaries. II. *Q. J. Mech. Appl. Maths* **32** (2), 125–133.

SAHOO, T. 2012 *Mathematical Techniques for Wave Interaction with Flexible Structures*. CRC Press, Taylor and Francis Group.

SAHOO, T., YIP, T.L. & CHWANG, A.T. 2001 Scattering of surface waves by a semi-infinite floating elastic plate. *Phys. Fluids* **13** (11), 3215–3222.

SCHULKES, R.M.S.M., HOSKING, R.J. & SNEYD, A.D. 1987 Waves due to a steadily moving source on a floating ice plate. Part 2. *J. Fluid Mech.* **180**, 297–318.

SHI, Y.Y., LI, Z.F. & WU, G.X. 2019 Interaction of wave with multiple wide polynyas. *Phys. Fluids* **31** (6), 067111.

SQUIRE, V.A. 2018 A fresh look at how ocean waves and sea ice interact. *Phil. Trans. R. Soc. Lond.* A **376** (2129), 20170342.

SQUIRE, V.A. 2020 Ocean wave interactions with sea ice: a reappraisal. *Annu. Rev. Fluid Mech.* **52**, 37–60.

SQUIRE, V.A. & DIXON, T.W. 2000 An analytic model for wave propagation across a crack in an ice sheet. *Intl J. Offshore Polar Engng* **10** (03), ISOPE-00-10-3-173.

SQUIRE, V.A., HOSKING, R.J., KERR, A.D. & LANGHORNE, P.J. 2012 *Moving Loads on Ice Plates*, vol. 45. Springer Science & Business Media.

WILLIAMS, T.D.C. 2006 Reflections on ice: scattering of flexural gravity waves by irregularities in arctic and antarctic ice sheets. PhD thesis, University of Otago.

XIA, D., KIM, J.W. & ERTEKIN, R.C. 2000 On the hydroelastic behavior of two-dimensional articulated plates. *Mar. Struct.* **13** (4–5), 261–278.